Available online at www.sciencedirect.com
ScienceDirect
Lithos 92 (2006) 154–180
LITHOS
www.elsevier.com/locate/lithos

Experimental constraints on the Skaergaard liquid line of descent

P. Thy [a,*], C.E. Lesher [a], T.F.D. Nielsen [b], C.K. Brooks [c]

[a] Department of Geology, University of California, One Shields Avenue, Davis, CA 95616, USA
[b] Geological Survey of Denmark and Greenland, Øster Voldgade 10, DK-1350 København K, Denmark
[c] Geologisk Institut, Københavns Universitet, Øster Voldgade 10, DK-1350 København K, Denmark

Received 1 July 2005; accepted 27 March 2006
Available online 6 June 2006

Abstract

New experimental information permits a forward approach to modeling the liquid line of descent of the Skaergaard intrusion. A series of melting experiments on chilled margins of evolved tholeiitic and ferrobasaltic dikes associated with the intrusion is, in combination with existing data, used to develop quantitative crystallization models that allow liquid and solid compositions to be predicted for initial magma compositions and crystallization conditions open or closed with respect to oxygen. The new experimental results comprise 6 experiments with melts coexisting with plagioclase and olivine, 29 experiments in addition containing augite, 14 experiments in addition containing ilmenite and/or magnetite, and 6 experiments in addition containing pigeonite and sometimes lacking olivine. All melting experiments were done at atmospheric pressure and with a furnace gas mostly controlled to the fayalite-magnetite-quartz oxygen buffer (FMQ).

Using these experimental results, the melt evolution can be constrained for the layered series of the Skaergaard intrusion. Fractionation of a LZa troctolitic assemblage drives the residual liquid toward increasing iron with slight increase in silica. The appearance of augite as an abundant mineral phase in the LZb and the fractionation of a gabbroic assemblage adjust the liquid trend to one of slightly decreasing silica with continued strong increase in iron. Silica decline is principally dependent on the crystallization of augite and restricted to LZb. The appearance of Fe–Ti oxide minerals and the fractionation of Fe–Ti oxide gabbroic assemblages in LZc deflect the evolution trends of iron and silica. The modeling based on the experimental results suggests marked LZc–MZ silica enrichment concurrently with increasing iron content until upper MZ and thereafter relatively constant or slightly decreasing iron.

The iron concentration level at which the deflection in iron and silica contents occurs is dependent on several factors of which the oxygen fugacity (f_{O_2}) has the strongest effect. Because of the restricted variation in f_{O_2} modeled in LZ (~0.1 log unit above FMQ), the saturation of oxide minerals and the liquid line of descent are unlikely to deviate strongly from the predicted variation based on open system experimental conditions. For the same reason, there is no support for the suggestion that widely different LZc oxide mineral modes will result from crystallization conditions closed with respect to oxygen as opposed to the experimental conditions.

Modeling based on the new experimental result suggests that iron can continue to increase through LZc, past the appearance of Fe–Ti oxides, and supports the possibility that iron may have continued to increase well into MZ. However, the forward modeling supports only a modest MZ and UZ decrease in f_{O_2} (<1 log unit below FMQ). This result is supported by a good correspondence between the experimental modes and the actual observed gabbro modes. A marked UZ drop in f_{O_2} (~2–3 log units below FMQ), as has been suggested, requires relatively high total modal content of Fe–Ti oxides (>20 wt.%) and dominating magnetite over ilmenite not permitted based on the experimental observations. Such high oxide modes will always result in liquid lines of descent

* Corresponding author.
E-mail address: thy@geology.ucdavis.edu (P. Thy).

0024-4937/$ - see front matter © 2006 Elsevier B.V. All rights reserved.
doi:10.1016/j.lithos.2006.03.031

that are characterized by strong enrichment in silica with strong depletion in iron. The forward modeling illustrates that only for unrealistic small amounts of Fe–Ti oxide minerals will iron enrichment accompany silica depletion into UZ.
© 2006 Elsevier B.V. All rights reserved.

Keywords: Layered intrusions; Skaergaard intrusion; Experimental constraints; Closed system; Fractional crystallization; Gabbro; Liquid line of descent; Iron variation; Silica enrichment; Oxygen fugacity

1. Introduction

The Skaergaard intrusion represents an extreme example of fractional crystallization of a small basaltic magma chamber trapped in continental crust during Tertiary rifting of the North Atlantic (Wager and Deer, 1939). Today, more than half-a-century after Wager and Deer's discovery of the intrusion and their pioneering work, the nature of the fractionating processes and the evolution path of the Skaergaard magma are still controversial and subject for debate (Hunter and Sparks, 1987, 1990; McBirney and Naslund, 1990; McBirney, 1995; Tegner, 1997; Irvine et al., 1998; Jang et al., 2001; Ariskin, 2002).

The Skaergaard magma chamber crystallized slowly by the separation and accumulation of the solid fraction on the floor and margins. The marginal and upper border series (MBS and UBS) formed by crystallization along the walls and under the roof, respectively, while the layered series (LS) simultaneously accumulated upward from the floor of the chamber (Fig. 1). The base of the LS is not exposed and the unknown section is often referred to as the hidden zone (HZ). The crystallization fronts converged in the sandwich horizon (SH) and resulted in an extremely differentiated stratigraphic gabbro section. This gabbro section allows assessments of the melt evolution and modes of solidification. The principal manifestation of the evolving nature of the magma is a systematic enrichment in the contents, for example, of albite in plagioclase and fayalite in olivine. An equally important manifestation is a systematic appearance/disappearance of minerals with falling temperature. The latter observation allows the layered and border series to be divided into zones and subzones dependent on the principal constituent mineral assemblages that provide convenient reference points for the magmatic evolution (Fig. 1).

Despite the well-preserved gabbro sequences, no direct traces of liquid are preserved in the intrusion. Rare mineral aggregates contained in early formed minerals have been interpreted to represent melt inclusions (Hanghøj et al., 1995; Jakobsen et al., 2005). The liquid line of descent can thus best be inferred indirectly. Because Fe–Ti oxide minerals appear relatively early in the Skaergaard cumulates (LZc), a subsequent differentiation trend characterized by iron and titanium depletion and silica enrichments was predicted by Hunter and Sparks (1987, 1990). This prediction contrasts with the strong iron enrichment that has been suggested to continue well past the appearance of Fe–Ti oxides (Fig. 2; Wager and Deer, 1939; Wager, 1960; Wager and Brown, 1967; McBirney and Naslund, 1990; Morse, 1990; McBirney, 1995; Tegner, 1997; McBirney, 1998). Basaltic magma undergoing fractional crystallization typically shows, dependent on the availability of oxygen, an initial path of iron and titanium enrichment with moderate silica depletion, followed by late stage evolution towards strongly decreasing iron and increasing silica contents (Bowen, 1928; Fenner, 1929; Osborn, 1959; Presnall, 1966). This has been confirmed by experimental melting of ferrobasalts under conditions appropriate for oceanic magmas (Juster et al., 1989; Snyder et al., 1993; Thy and Lofgren, 1994; Toplis and Carroll, 1995). These

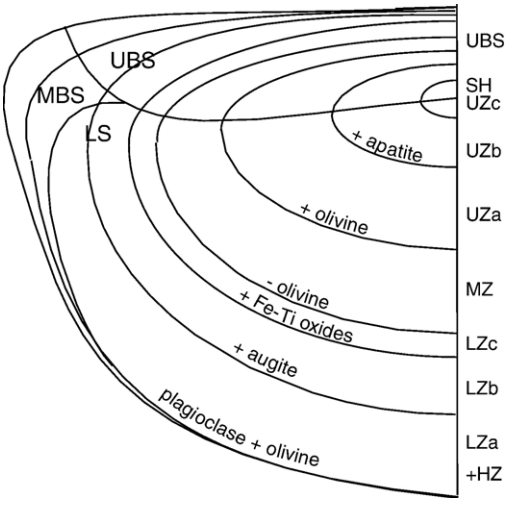

Fig. 1. Schematic representation of the margins and interior of the Skaergaard intrusion. Illustrated are the relative extent of the border series (Marginal Border Series, MBS, and Upper Border Series, UBS) and layered series (LS) with zone divisions and incoming/exit of mineral phases after Wager and Brown (1967), Naslund (1984), and Hoover (1989b). Additional abbreviations are Hidden Zone, HZ; Lower Zone, LZ; Middle Zone, MZ; Upper Zone, UZ, and Sandwich Horizon, SH.

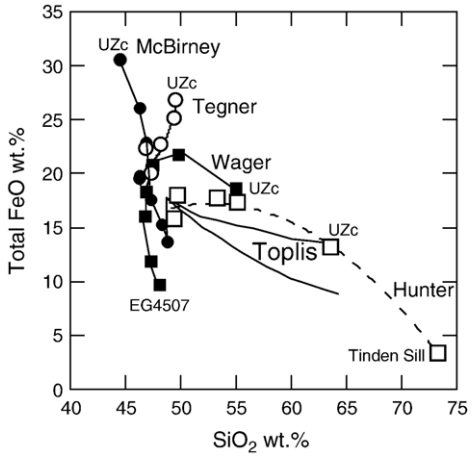

Fig. 2. Total FeO versus SiO_2 content in wt.% for some suggested liquid lines of descent for the Skaergaard magma (Wager, 1960; Hunter and Sparks, 1987; McBirney and Naslund, 1990; Toplis and Carroll, 1996; Tegner, 1997). The liquid lines marked 'Toplis' are for conditions open (lower curve) or closed (upper curve) with respect to oxygen (Toplis and Carroll, 1996). Estimates for UZc are indicated. EG4507 and Tinden Sill are from Wager (1960).

experimental results unambiguously demonstrate that the arrival of Fe–Ti oxide minerals ultimately drive the residual liquid toward iron depletion and silica enrichment. The experimental evidence thus suggests iron enrichments that are restricted by the crystallization of Fe–Ti oxide minerals. This is consistent with observations from Icelandic volcanic series (Carmichael, 1964; Wood, 1978; Hunter and Sparks, 1987; Macdonald et al., 1987, 1990; Nicholson et al., 1991; Furman et al., 1992).

Prediction of the Skaergaard liquid line of descent is dependent on several uncertainties. Most important of these are the problem of identifying the composition of the parental melt, the limitations in our understanding of the relevant experimental phase equilibria, and the compositional variability and volume relations of the cumulate sequence (Wager, 1960; Chayes, 1970; Irvine, 1970; McBirney, 1975; Ford, 1981; Hunter and Sparks, 1987; Toplis and Carroll, 1996; Ariskin, 1999, 2002; Nielsen, 2004). In this paper we focus on the experimental phase equilibria for likely Skaergaard parental melts. We present the detailed result of an experimental study (Thy and Lesher, 1993) of chilled margins from a dike swarm in the outer Kangerdlugssuaq Fjord area contemporaneous with the Skaergaard intrusion and the main phase of the Blosseville Kyst plateau lavas (Nielsen, 1978; Brooks and Nielsen, 1978, 1990). Together with previous experimental work on Skaergaard related compositions (Tilley et al., 1963; Biggar, 1974; Hoover, 1978, 1989a; Snyder et al., 1993; Toplis and Carroll, 1995), the present results are used to formulate a quantitative crystallization model that allows the liquid line of descent to be predicted for various physical conditions, crystallization and mineral modes, and compositions of the parental magma. We develop the crystallization model for understanding the possible liquid lines of descent of the Skaergaard intrusion and particularly the conditions for which protracted iron enrichment past saturation in Fe–Ti oxides is feasible.

The exploratory forward modeling of the Skaergaard magma illustrates that only for exceedingly small amounts of Fe–Ti oxide minerals in the solid fractionate will iron enrichment accompany silica depletion into UZ as suggested by McBirney (1995). Fractionation of Fe–Ti oxide mineral modes consistent with the experimental results drive the liquid line of descent toward enrichment in silica together with relatively constant or slightly decreasing iron content.

2. The Skaergaard dikes and sample selection

A central problem for any discussion of the liquid evolution of the Skaergaard intrusion is the identification of likely parental magma compositions that can be used as a starting point to model the liquid line of descent. The search for the parental magma has mainly been centered on identifying proper chilled samples from the marginal border groups (Wager, 1960; McBirney, 1975; Hoover, 1989a). The heterogeneous nature of the marginal zone of the Skaergaard intrusion and the possibility for crystal accumulation, crustal contamination, and alteration cause problems when attempting to identify suitable and unmistakable parental magma compositions (McBirney, 1975; Hoover, 1989a; McBirney, 1996). Consequently, Nielsen (1978) and Brooks and Nielsen (1978, 1990) focused their attention on the associated dike swarms in the outer Kangerdlugssuaq Fjord area and identified an early tholeiitic dike swarm (Wager and Deer, 1938; Brooks, 1979; Myers, 1980; Nielsen and Brooks, 1981). The dike swarm has variously been referred to as 'THOL-2' or 'FG-1 dikes,' but for ease we here simply refer to them as 'Skaergaard dikes.' Brooks and Nielsen (1978) suggested that these dikes were contemporaneous with the Skaergaard intrusion and associated macrodike intrusions. This dike swarm was mapped and sampled in detail on Kraemers Island (Nielsen, 1978). Brooks and Nielsen (1978) argued that this swarm represented Skaergaard-related magmas and the liquid line of descent of the intrusion.

Brooks and Nielsen (1978) sampled the central parts of the dikes and identified five compositional groups that were referred to as *A, B, C, D,* and *E* in order of decreasing $Mg/(Mg+Fe^{2+})$ ratios (Table 1). The dikes are evolved ferrobasalts and range from a group with relatively high SiO_2 (48–50 wt.%), $Mg/(Mg+Fe^{2+})$ ratios between 0.70 and 0.50, and TiO_2 between 1.5 and 3 wt.% to a more evolved group characterized by lower SiO_2 (46–47 wt.%), $Mg/(Mg+Fe^{2+})$ ratios below 0.45, and TiO_2 between 4 and 6 wt.% (Fig. 3). The dikes are in many respects similar to the lavas of Geikie Plateau Formation of the East Greenland plateau basalts (Larsen et al., 1989; Nielsen, 2004; Andreasen et al., 2004). Subsequent to the discussion of the Skaergaard liquid line of descent by Hunter and Sparks (1987), Brooks and Nielsen (1990) re-sampled the dikes from their marginal parts in order to avoid the possible effects of crystal accumulation. These samples are here designated as '*m*' for margins and '*c*' for centers of dikes. Across-dike profiles suggest that both sampling sets, perhaps with the exception of dike *A*, reflect the intruded magmas without effects of crystal accumulation. Most of the experiments discussed in this paper were performed on the three dike margin samples (*Am, Bm, Cm*) and one interior sample (*Dc*). Of these, samples *Am* and *Bm* have nearly identical $Mg/(Mg+Fe^{total})$ ratios (0.51), *Cm* and *Dc* have lower ratios of 0.45 and 0.41, respectively. The variation in $Mg/(Mg+Fe^{2+})$ ratios is negatively correlated with TiO_2 contents of the dikes (Fig. 3). A subset of experiments at an oxygen fugacity (f_{O_2}) one log-unit below the FMQ buffer were performed on samples *Ac*, *Bc*, and *Cc*. The new experimental results greatly expand the available Skaergaard-related database of Toplis and Carroll (1995). Toplis and Carroll (1995) used a synthetic equivalent of dike *Cc* lacking P_2O_5 and MnO (Table 1, SC1) for their study of the effects of oxygen fugacity (see Toplis et al. (1994) for a study of the effect of adding P_2O_5 to SCI). Experimental work on Skaergaard chilled margin samples (Table 1, Fig. 2) have also previously been presented by Tilley et

Table 1
Composition of Skaergaard dikes, related compositions, and analytical precision

	Am	Ac	Bm	Bc	Cm	Cc	Dc	Em	Ec	EG-4507	KT39	SC1	W-1 $N=51$	W-1 S.D.	W-1 Recom.
SiO_2	48.04	48.26	48.13	48.11	48.25	48.34	47.91	45.13	45.11	48.08	50.10	48.8	52.72	0.25	52.46
TiO_2	2.05	1.35	2.07	1.75	2.92	2.92	4.36	4.98	5.41	1.17	2.64	2.9	1.22	0.11	1.07
Al_2O_3	13.96	15.34	13.90	14.70	13.34	13.13	12.42	12.09	11.88	17.22	13.40	14.9	15.15	0.15	15.00
FeO	12.27	8.87	12.33	10.95	13.69	13.14	14.74	16.06	16.28	9.62	13.39	13.1	10.81	0.24	10.06
MnO	0.19	0.15	0.19	0.17	0.20	0.22	0.23	0.22	0.26	0.16	0.20		0.17	0.06	0.17
MgO	7.12	8.07	7.08	7.44	6.31	6.40	5.79	5.97	5.19	8.62	6.54	6.5	6.56	0.10	6.62
CaO	11.54	12.88	11.50	11.71	10.70	10.87	9.29	9.70	10.04	11.38	10.10	10.9	10.68	0.21	11.00
Na_2O	1.90	2.08	2.29	2.31	2.46	2.44	2.59	2.47	2.60	2.37	2.42	2.7	2.30	0.08	2.16
K_2O	0.82	0.24	0.41	0.31	0.45	0.39	0.58	0.69	0.73	0.25	0.57	0.3	0.62	0.04	0.64
P_2O_5	0.19	0.16	0.19	0.19	0.29	0.35	0.64	0.77	0.10	0.22	0.15		0.08	0.13	
L.O.I.	1.26	1.03	1.30	1.66	1.29	1.00	0.52	1.39	0.89	1.06					
Total	99.34	98.43	99.39	99.30	99.76	99.20	98.79	99.34	99.16	100.03	99.58	100.1	100.38		99.31
Mg#	0.508	0.619	0.506	0.548	0.451	0.467	0.412	0.399	0.362	0.614	0.465	0.469			
CIPW weight norm															
or	4.94	1.46	2.47	1.88	2.70	2.35	3.49	4.16	4.39	1.49	3.38	1.77			
ab	16.39	18.07	19.75	20.02	21.11	21.01	22.30	21.34	22.39	20.26	20.56	22.82			
an	27.66	32.65	26.94	29.51	24.36	24.13	20.91	20.27	18.91	35.97	24.11	27.62			
hy	11.80	8.26	10.03	9.37	14.23	15.91	20.96	9.37	7.71	5.05	22.92	8.49			
di	24.44	26.09	24.87	23.71	23.01	23.68	19.75	20.60	22.44	16.73	20.65	21.98			
ol	10.35	10.46	11.48	11.65	8.29	6.46	3.32	13.08	11.90	18.02	2.8	11.82			
il	3.97	2.63	4.01	3.40	5.62	5.64	8.43	9.66	10.46	2.25	5.04	5.50			
ap	0.46	0.39	0.46	0.46	0.70	0.84	0.87	1.55	1.86	0.24	0.52				

Am is from Brooks and Nielsen (1990), their sample "1" (MM40533); *Ac* is from Brooks and Nielsen (1978), their sample "A" (MM27700-2); *Bm* is from Brooks and Nielsen (1990), their sample "2" (MM40534); *Bc* is from Brooks and Nielsen (1978), their sample "B" (MM27695); *Cm* is from Brooks and Nielsen (1990), their sample "3" (MM40436); *Cc* is from Brooks and Nielsen (1978), their sample "C" (MM27700-16); *Dc* is from Brooks and Nielsen (1978), their sample "D" (MM27633); *Em* is from Brooks and Nielsen (1990), their sample '4' (MM40532); *Ec* is from Brooks and Nielsen (1978), their sample 'E' (MM27700-34). The analyses given by Brooks and Nielsen (1990) differ only slightly from the present reanalyzed powders. Analysis EG-4207 is from Wager (1960), KT39 from Hoover (1989a), and SC1 from Toplis and Carroll (1995). Mg# = Mg/(Mg+Fe) and CIPW weight norm are calculated with all iron as FeO. W-1 is fused international reference sample W-1 given as an average of 51 point microprobe analyses ($N=51$), one standard deviation (S.D.), and recommended value (Recom.) from Govindaraju (1989).

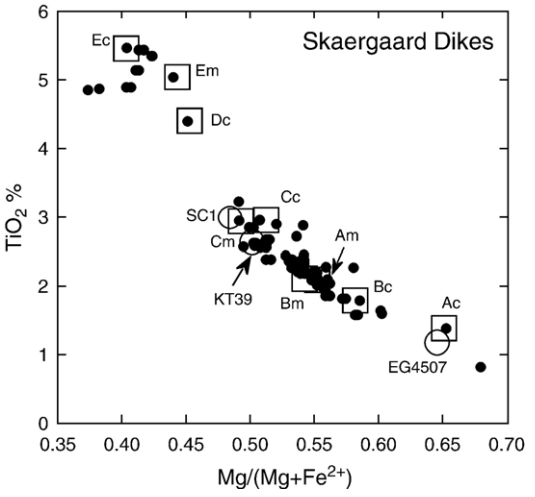

Fig. 3. TiO_2 % versus $Mg/(Mg+Fe^{2+})$ ratio for existing analyses of Skaergaard dikes (dark dots). Boxes and circles show the samples used or discussed in this study (Table 1). Fe^{3+}/Fe^{2+} has been calculated according to Kilinc et al. (1983).

al. (1963; *EG4507*), Biggar (1974; *EG4507*), Hoover (1978, 1989a; *KT–39*), and Snyder et al. (1993; *KT–39*).

3. Experimental and analytical techniques

3.1. Sample preparation and experiments

The dike samples were ground in a tungsten-carbide shatter box for about two minutes and subsequently in an agate mortar under acetone to an estimated maximum grain size of about 10 μm. About 0.5 g of powder for each sample were mixed with an organic binder (polyvinyl alcohol) and pressed into pellets. These pellets were broken to approximately 50 mg-size pieces and sintered to 0.004 in. diameter FePt alloy wire prepared by iron-plating and annealing Pt wire to produce an alloy in equilibrium with the experimental products (Grove, 1981). The experimental charges were suspended in a vertical quench furnace at atmospheric pressure (Williams and Mullins, 1981). Temperature was monitored by a $Pt/Pt^{90}Rh^{10}$ thermocouple calibrated against the melting point of gold (Biggar, 1972). For most experiments, the furnace atmosphere was controlled to the fayalite-magnetite-quartz (FMQ) oxygen buffer by a $CO–CO_2$ gas mixture (~3–4 cm^3/s flow rate) and monitored by a solid ZrO_2-ceramic oxygen probe calibrated against the Ni–NiO reaction. A small subset of experiments was conducted at one log-unit below the FMQ oxygen buffer (Table 2). The f_{O_2} measured prior to start of the individual experiment is listed in Table 2. The duration of experiments varied from 22 h near the liquidus to 228 h near the solidus. All experiments were quenched in air. The temperature interval between experiments was typically about 10 °C, giving an uncertainty in the locations of phase boundaries of approximately ±5 °C. The experimental conditions and results are summarized in Table 2.

3.2. Electron microprobe analyses

The phase compositions were determined using a Cameca SX-50 electron microprobe with an acceleration voltage of 15 kV, a beam current of 10 nA, and counting times between 10 and 30 s. All phases were analyzed using natural minerals as standards. A beam diameter of 1–2 μm was used to analyze all minerals, while most glasses were analyzed with a 10 μm broad beam to minimize volatilization of sodium. A focused beam, however, was used to analyze small melt pools in the lowest temperature experiments. An internal glass standard prepared from international rock standard W-1 (Govindaraju, 1989) was analyzed concurrently as a control and measure of analytical precision and accuracy (Table 1). The proportion of ferric and ferrous iron in liquids at the run conditions was estimated using the equations of Kilinc et al. (1983). These recalculated FeO concentrations are used throughout the paper unless otherwise stated.

The experimental products were routinely examined by back-scattered electron (BSE) images prior to analysis. This visual information, in addition to the compositional data, allows an evaluation of the homogeneity of silicate minerals and glasses, and the equilibration in the products. As a standard analytical procedure, grains that morphologically reflect disequilibrium with unreacted parts or patchy zoning, judging from the mean-atomic-density BSE images, were typically avoided or only their marginal parts analyzed. We also attempted to avoid the smallest and largest grains, restricting analysis to grains between 20 and 100 μm in diameter most likely to have grown from the coexisting liquid. The resulting analyses were screened by compositional and stoichiometrical criteria and are considered representative for the experimental products. The average compositions of glasses and minerals for each experimental product are reported in Table 3 and Supplementary Dataset 1–4 (Tables 4–7), respectively. The Supplementary Dataset is available in the online version at http://www.sciencedirect.com; see Appendix B.

Despite our attempts to analyze only equilibrium grains, compositional heterogeneity is still reflected in the standard deviations of replicate analyses. The standard deviation of the experimental glasses is, for most experimental products with relatively high amounts of glass, comparable with the analytical precision (Tables 1

Table 2
Experimental conditions and results

Run. no.	T °C	f_{O_2} log	Duration hours	Phase assemblage	Phase proportions							Na_2O loss	R^2
					liq	ol	pl	cpx	il	mt	pig		
FG1-Am													
1-14	1182	−8.81	25	gl	1.000								
1-13	1173	−8.67	22	gl ol pl	0.861	0.037	0.102						0.294
1-9	1163	−8.94	30	gl ol pl cpx	0.802	0.036	0.115	0.047					0.082
1-8	1154	−8.94	42	gl ol pl cpx	0.723	0.045	0.156	0.076					0.077
1-6	1144	−9.30	23	gl ol pl cpx	0.618	0.053	0.200	0.129					0.147
1-4	1135	−9.36	24	gl ol pl cpx	0.561	0.061	0.220	0.158					0.025
1-3	1126	−9.50	67	gl ol pl cpx	0.496	0.064	0.247	0.193					0.051
1-2	1117	−9.53	92	gl ol pl cpx	0.431	0.080	0.278	0.211				0.10	0.073
1-1	1106	−9.72	88	gl ol pl cpx	0.388	0.078	0.297	0.237				0.10	0.071
1-7	1097	−9.90	95	gl ol pl cpx mt	0.288	0.076	0.346	0.285		0.005			0.183
1-11	1089	−9.95	118	gl ol pl cpx il mt	0.205	0.071	0.377	0.325	0.014	0.008		0.10	0.121
1-12	1078	−10.10	228	gl ol pl cpx il mt pig	0.142	0.062	0.404	0.358	0.016	0.018	<0.005	0.10	0.105
FG1-Ac													
EG-5	1201	−9.64	27	gl ol pl cpx	0.761	0.021	0.141	0.077					0.012
EG-4	1179	−10.00	36	gl ol pl cpx	0.591	0.041	0.226	0.142				0.10	0.026
EG-1	1161	−10.16	41	gl ol pl cpx	0.400	0.060	0.319	0.221				0.20	0.061
EG-2	1138	−10.53	77	gl ol pl cpx	0.234	0.084	0.403	0.279				0.10	0.062
EG-3	1116	−10.78	100	gl ol pl cpx il	0.078	0.087	0.475	0.351	0.009			0.10	0.257
FG1-Bm													
1-14	1182	−8.81	25	gl	1.000								
1-13	1173	−8.67	22	gl ol pl	0.873	0.030	0.097					0.10	0.339
1-10	1163	−8.94	24	gl ol pl cpx	0.794	0.033	0.122	0.051				0.10	0.061
1-8	1154	−8.94	42	gl ol pl cpx	0.704	0.036	0.163	0.097				0.10	0.023
1-6	1144	−9.30	23	gl ol pl cpx	0.620	0.042	0.205	0.133				0.20	0.025
1-4	1135	−9.36	24	gl ol pl cpx	0.555	0.050	0.236	0.159					0.024
1-3	1126	−9.50	67	gl ol pl cpx	0.459	0.059	0.277	0.205				0.10	0.013
1-2	1117	−9.53	92	gl ol pl cpx	0.414	0.072	0.296	0.218				0.10	0.085
1-1	1106	−9.72	88	gl ol pl cpx	0.361	0.063	0.321	0.255				0.20	0.071
1-7	1097	−9.90	95	gl ol pl cpx il mt	0.262	0.064	0.357	0.305	0.012	<0.005		0.20	0.539
1-11	1089	−9.95	118	gl ol pl cpx il mt pig	0.157	0.060	0.404	0.356	0.016	0.007	<0.005	0.30	0.032
FG1-Bc													
EG-5	1201	−9.64	27	gl ol pl	0.883	0.023	0.094					0.30	0.325
EG-1	1161	−10.16	41	gl ol pl cpx	0.550	0.067	0.255	0.128				0.30	0.175
EG-3	1116	−10.78	100	gl ol pl cpx	0.242	0.076	0.393	0.289				0.30	0.199
FG1-Cm													
1-13	1173	−8.67	22	gl	1.000								
1-19	1168 *	−8.89	29	gl pl									
1-10	1163	−8.94	24	gl pl	0.939		0.061						1.429
1-8	1154	−8.94	42	gl pl	0.927		0.073						1.429
1-6	1144	−9.30	23	gl ol pl cpx	0.792	0.020	0.119	0.069					0.348
1-4	1135	−9.36	24	gl ol pl cpx	0.658	0.036	0.189	0.117					0.352
1-3	1126	−9.50	67	gl ol pl cpx	0.608	0.040	0.219	0.133					0.307
1-2	1117	−9.53	92	gl ol pl cpx	0.557	0.048	0.243	0.152					0.325
1-18	1107	−9.80	24	gl ol pl cpx	0.474	0.068	0.293	0.165				0.20	0.352
1-7	1097	−9.90	95	gl ol pl cpx il	0.350	0.063	0.342	0.230	0.015			0.20	0.244
1-11	1089	−9.95	118	gl ol pl cpx il mt pig	0.291	0.019	0.347	0.255	0.026	<0.005	0.062	0.20	0.014
1-12	1078	−10.10	228	gl pl cpx il mt pig	0.123		0.412	0.312	0.021	0.044	0.088		0.049

(continued on next page)

Table 2 (*continued*)

Run. no.	T °C	f_{O_2} log	Duration hours	Phase assemblage	Phase proportions							Na_2O loss	R^2
					liq	ol	pl	cpx	il	mt	pig		
FG1-Cc													
EG-4	1179	−10.00	36	gl	1.000								
EG-1	1161	−10.25	41	gl ol pl	0.929	0.013	0.058						0.386
FG1-Cc													
EG-2	1138	−10.53	77	gl ol pl cpx	0.669	0.036	0.176	0.119				0.10	0.085
EG-3	1116	−10.78	100	gl ol pl cpx il	0.459	0.060	0.287	0.194	<0.005			0.20	0.283
FG1-Dc													
1-8	1154	−8.94	42	gl	1.000								
1-6	1144	−9.30	23	gl pl	1.000		<0.005						
1-4	1135	−9.36	24	gl ol pl	0.926	0.021	0.053						0.371
1-3	1126	−9.50	67	gl ol pl	0.866	0.039	0.095						0.421
1-2	1117	−9.53	92	gl ol pl cpx	0.799	0.044	0.122	0.035				0.10	0.175
1-1	1106	−9.72	88	gl ol pl cpx	0.763	0.039	0.130	0.068				0.10	0.217
1-7	1097	−9.90	95	gl ol pl cpx il	0.474	0.066	0.291	0.138	0.031			0.40	1.549
1-11	1089	−9.95	118	gl ol pl cpx il mt pig	0.426	<0.005	0.278	0.153	0.048	<0.005	0.095	0.50	0.077
1-12	1078	−10.10	228	gl pl cpx il mt pig	0.278		0.337	0.192	0.051	0.023	0.118	0.30	0.026
EG-4	1179	−10.00	36	gl	1.000								
EG-2	1138	−10.53	77	gl ol pl cpx	0.851	0.032	0.096	0.021				0.20	1.188
EG-3	1116	−10.78	100	gl ol pl cpx il	0.730	0.054	0.152	0.060	0.004			0.20	0.075

liq, liquid; cpx, high-Ca pyroxene; pl, plagioclase; ol, olivine; il, ilmenite; mt, titanomagnetite; pig, low-Ca pyroxene.
Phase proportions (wt.%) have been estimated by least-squares mixing calculations and the determined phase compositions of Tables 3–8. Na_2O loss (wt.%) has been estimated by including Na_2O as a mineral. R^2 is the sum of the squares of the residuals of the mixing calculations.
* Held for 30 min above liquidus (1177 °C) and then lowered to run temperature (1168 °C) with a ramp rate of 500 °C/hours.

and 3). Similarly, olivine is well homogenized within a given experimental product (Supplementary Dataset 1 (Table 4)). Plagioclase (Supplementary Dataset 2 (Table 5)) and augite (Supplementary Dataset 3 (Table 6)) are more variable in composition with both decreasing temperature and melt fraction. Because the experiments are melting experiments, the original grains must either melt or reequilibrate during the duration of the experiment. Consequently, the highest proportion of unequilibrated grains occurs as expected in the lowest temperature runs. This results in biases of the average mineral compositions toward that of the starting material and complicates the interpretation and application of the low temperature experimental results.

3.3. Modal abundance and elemental losses

The modes of the experimental charges are estimated by weighted mass balance calculations using the compositions of the phases determined by electron microprobe (Bryan et al., 1969). All oxides were assigned a weighting factor of 1.0, except SiO_2 and Al_2O_3 that were weighted 0.4 and 0.5, respectively. The sums of squares of residuals given in Table 2 are based on these weighted calculations.

Iron deficiencies were not detected by the mass balance calculations and the iron content of the hang wire appears to have been appropriate to prevent resolvable loss or gain. The iron loss of sodium to the furnace gas and under the electron microbeam are estimated by the mass balance and are typically less than 5% relative, but may exceed 15% for some low temperature and long duration experiments that were analyzed using a focused beam. These losses of sodium are corrected for in Table 3 by adding the calculated loss (Table 2) to the analytical results (Table 3).

4. Experimental results

4.1. Phase appearances

The experimental results on Skaergaard dike compositions are summarized in Table 2 in terms of melting temperature and in Fig. 4 as a function of the Mg/(Mg+Fe^{total}) ratio of starting compositions. The two most primitive samples *Am* and *Bm* show near identical crystallization orders with olivine and plagioclase appearing simultaneously at 1178±5 °C, augite at 1168±5 °C, Fe–Ti oxides at 1102±5 °C, and pigeonite between 1084 °C and 1093 °C. With decreasing Mg/(Mg+Fe^{total}) ratio of the starting compositions, the

liquidus is significantly lowered and the first phase to appear on the liquidus is plagioclase followed by olivine (*Dc*) or by co-precipitation of olivine and augite (*Cm*). Sample *Cm* shows a considerable liquidus melting interval for plagioclase (~20 °C) prior to simultaneous appearance of olivine and augite at 1149 °C. The temperature for the appearance of Fe–Ti oxide minerals is nearly identical for the four compositions (1102±5 °C). Pigeonite appears at a temperature of 1093±4 °C for compositions *Bm, Cm*, and *Dc* and olivine disappears at 1084±6 °C for *Cm* and *Dc*.

In summary, the relatively primitive samples show a small liquidus interval of coprecipitating plagioclase and olivine (~10 °C) before they are multiply saturated in olivine, plagioclase, and augite. The relatively evolved samples, however, show a small liquidus interval for plagioclase-only before olivine and subsequently augite appears. The results for our sample *Cc* are comparable with those of Toplis and Carroll (1995) on a synthetic material (SC1) based on the same composition (Table 1). Toplis and Carroll (1995) reported olivine and plagioclase cosaturation at 1162 °C, the appearance of augite at 1130 °C, and Fe–Ti oxides at 1100 °C. Compared to the present results on sample *Cm*, Toplis and Carroll (1995) obtained a significantly earlier saturation of olivine and later augite saturation.

4.2. Phase proportions

The calculated phase proportions at each stage of melting (Table 2) are shown as a function of liquid fraction in Fig. 5. The proportion of augite increases slightly faster than the proportion of plagioclase with advancing solidification. Olivine increases only slightly with decreasing melt fraction until the appearance of pigeonite and disappears after the stabilization of pigeonite in *Cm* and *Dc* experiments. The modal contents of Fe–Ti oxide minerals are consistently low and without clear correlation with the remaining liquid (Table 2).

The absolute amount of pigeonite and olivine is difficult to assess due to the low amounts and uncertainties in determining equilibrium compositions in low temperature experiments. Despite this uncertainty, the low temperature multiple saturated liquids for dikes *Cm* and *Dc* may represent a reaction boundary at which olivine reacts with the liquid to form pigeonite. The coefficients for this reaction, terminating the coexistence of olivine and liquid is 0.9 liquid+0.1 olivine=0.2 pigeonite+0.4 plagioclase+0.4 augite. These calculated coefficients for olivine and pigeonite are significantly lower than those given by Grove and Baker (1984) and Juster et al. (1989) for similar reactions in more magnesium rich basalts (Grove et al., 1982; Grove and Bryan, 1983) and olivine-seeded Fe–Ti basalts (Juster et al., 1989).

The total modes obtained at about 15% liquid remaining are nearly identical for samples *Am* and *Bm* with 7% olivine, 47% plagioclase, 42% augite, 2% ilmenite, 2% magnetite. Pigeonite is present in these experiments in trace amounts. With 10–30% liquid remaining, the evolved *Cm* and *Dc* samples reached a total mode of 47% plagioclase, 27–36% augite, 10–16% pigeonite, 2–7% ilmenite, 3–5% magnetite, and were without olivine.

The experiments of Toplis and Carroll (1995) show for olivine, plagioclase, and augite saturated melts lower modal proportion of augite and higher plagioclase (13% olivine, 57% plagioclase, and 27% augite). This may reflect the higher Al_2O_3 content in the starting material used by Toplis and Carroll (1995) that may result in relatively higher plagioclase modes. In addition, their starting composition was not saturated in low-Ca pyroxenes for the investigated temperature interval. This lack of low-Ca pyroxene was attributed by Toplis et al. (1994) to the effect of not including P_2O_5 in the SC1 starting composition.

4.3. Phase compositions

Compositions of the experimental liquids are given in Table 3. The concentrations of most oxides show systematic variations with temperature and liquid/solid fractions. For example, the MgO content (wt.%) of the liquid correlates well with its temperature, yielding an empirical geothermometer given by T (°C)=995.35+26.365*MgO ($\sum R^2=0.989$; standard error 4.5 °C) for all experiments on the FMQ oxygen buffer (Fig. 6). Similarly, most oxide concentrations show systematic variation as a function of MgO content (Fig. 7). The oxides Al_2O_3 and CaO show systematic decreases with decreasing MgO because of the dominant plagioclase and augite crystallization. The early crystallization of plagioclase, or plagioclase and olivine, has little detectable effects on the liquid lines of descent due to the relatively short temperature intervals these phases alone are on the liquidus. The incompatible oxides TiO_2 and K_2O show marked increases with advancing stages of crystallization. Na_2O show little variation and appears constant or decreases slightly with decreasing MgO (Table 3).

Glass of all melted samples show initially slightly decreasing or constant SiO_2 with increasing FeO and

Table 3
Composition of experimental glasses

Run no.	T °C	N	SiO_2	TiO_2	Al_2O_3	FeO*	MnO	MgO	CaO	Na_2O	K_2O	P_2O_5	Na_2O corr.	Mg#	1 standard deviation									
															SiO_2	TiO_2	Al_2O_3	FeO	MnO	MgO	CaO	Na_2O	K_2O	P_2O_5
FG1-Am																								
1-14	1182	11	48.73	2.18	14.15	12.87	0.22	7.07	11.58	1.89	0.71	0.19		0.495	0.27	0.09	0.17	0.38	0.03	0.10	0.25	0.07	0.04	0.04
1-13	1173	8	48.49	2.33	13.72	13.71	0.24	6.65	11.74	1.92	0.75	0.20		0.464	0.29	0.11	0.15	0.15	0.05	0.11	0.16	0.09	0.03	0.07
1-9	1163	7	48.57	2.41	13.51	14.00	0.25	6.39	11.52	1.92	0.81	0.21		0.449	0.10	0.10	0.14	0.21	0.05	0.12	0.09	0.05	0.05	0.07
1-8	1154	10	48.13	2.63	13.01	14.48	0.24	5.95	11.12	1.92	0.83	0.24		0.423	0.16	0.14	0.17	0.30	0.05	0.13	0.12	0.05	0.06	0.09
1-6	1144	7	48.86	2.73	12.93	15.51	0.23	5.63	10.80	1.91	0.83	0.25		0.393	0.37	0.11	0.11	0.27	0.03	0.10	0.11	0.05	0.06	0.06
1-4	1135	6	48.13	3.22	12.72	15.59	0.20	5.06	10.25	2.02	1.20	0.34		0.366	0.37	0.08	0.18	0.24	0.02	0.12	0.18	0.06	0.06	0.07
1-3	1126	7	48.22	3.43	12.53	16.37	0.24	4.81	9.94	2.02	1.25	0.32		0.344	0.72	0.10	0.16	0.22	0.07	0.10	0.18	0.08	0.03	0.06
1-2	1117	7	48.63	3.91	12.19	16.54	0.21	4.21	9.49	1.95	1.36	0.34	2.05	0.312	0.37	0.08	0.18	0.46	0.06	0.08	0.08	0.05	0.04	0.08
1-1	1106	8	48.78	4.32	12.08	16.76	0.24	4.13	9.18	1.90	1.42	0.36	2.00	0.305	0.31	0.08	0.26	0.38	0.04	0.12	0.12	0.08	0.05	0.06
1-7	1097	7	48.99	4.53	11.55	17.32	0.26	3.81	8.76	1.88	1.41	0.47		0.282	0.19	0.15	0.13	0.20	0.03	0.06	0.18	0.08	0.04	0.04
1-11	1089	9	52.33	3.82	11.88	17.26	0.30	3.41	8.06	1.87	1.77	0.61	1.97	0.260	0.58	0.06	0.22	0.51	0.04	0.08	0.23	0.11	0.07	0.12
1-12	1078	4	52.61	3.28	11.95	15.64	0.24	2.77	7.60	1.78	2.23	0.91	1.88	0.240	0.50	0.09	0.28	0.53	0.07	0.06	0.11	0.05	0.07	0.05
FG1-Ac																								
EG-5	1201	7	49.88	1.69	14.57	10.89	0.27	7.99	12.64	2.24	0.25	0.17		0.567	0.15	0.07	0.17	0.34	0.05	0.13	0.15	0.13	0.02	0.05
EG-4	1179	10	49.44	2.20	13.93	11.90	0.20	7.15	12.17	2.12	0.30	0.20	2.22	0.517	0.35	0.08	0.14	0.35	0.06	0.20	0.11	0.06	0.02	0.04
EG-1	1161	8	48.62	2.79	12.93	13.91	0.20	6.07	10.66	2.41	0.43	0.28	2.61	0.438	0.51	0.08	0.21	0.30	0.06	0.09	0.14	0.08	0.04	0.07
EG-2	1138	5	48.07	4.03	12.04	15.89	0.28	4.81	9.61	2.25	0.69	0.44	2.35	0.350	0.60	0.37	0.54	0.57	0.09	0.21	0.10	0.15	0.04	0.04
EG-3	1116	13	48.65	4.48	11.57	16.80	0.27	4.23	8.94	2.00	0.88	0.71	2.10	0.310	0.86	0.24	0.47	0.53	0.07	0.31	0.22	0.15	0.06	0.16
FG1-Bm																								
1-14	1182	11	48.15	2.19	13.94	13.28	0.22	7.09	11.54	2.24	0.37	0.18		0.488	0.30	0.10	0.15	0.32	0.04	0.10	0.13	0.08	0.03	0.04
1-13	1173	7	48.49	2.32	13.62	13.81	0.24	6.78	11.59	2.25	0.37	0.19	2.35	0.467	0.26	0.12	0.10	0.41	0.03	0.16	0.21	0.13	0.02	0.08
1-10	1163	7	48.22	2.52	13.13	14.12	0.26	6.39	11.43	2.24	0.43	0.24	2.34	0.446	0.25	0.03	0.14	0.30	0.05	0.09	0.19	0.09	0.03	0.06
1-8	1154	7	48.40	2.68	12.69	14.99	0.30	6.04	10.97	2.33	0.47	0.22	2.43	0.418	0.21	0.13	0.08	0.37	0.02	0.11	0.14	0.10	0.06	0.03
1-6	1144	8	47.99	2.99	12.43	15.96	0.26	5.69	10.75	2.18	0.47	0.27	2.38	0.389	0.34	0.14	0.11	0.47	0.03	0.12	0.13	0.08	0.02	0.05
1-4	1135	6	47.80	3.26	12.18	16.47	0.26	5.33	10.41	2.26	0.63	0.29		0.366	0.46	0.09	0.17	0.26	0.05	0.13	0.19	0.05	0.04	0.06
1-3	1126	4	47.69	3.86	11.78	17.25	0.27	4.78	9.94	2.35	0.73	0.31	2.45	0.331	0.22	0.01	0.31	0.56	0.03	0.12	0.10	0.19	0.07	0.05
1-2	1117	5	47.36	4.37	11.45	17.26	0.26	4.31	9.76	2.22	0.71	0.43	2.32	0.308	0.17	0.19	0.07	0.31	0.06	0.08	0.17	0.08	0.06	0.03
1-1	1106	5	47.05	4.92	11.04	18.79	0.31	4.53	9.43	2.06	0.70	0.49	2.26	0.301	0.22	0.11	0.19	0.13	0.04	0.06	0.06	0.08	0.04	0.08
1-7	1097	6	47.90	4.87	10.57	18.35	0.30	3.85	8.71	1.89	0.80	0.61	2.09	0.272	0.29	0.18	0.19	0.36	0.06	0.13	0.13	0.08	0.02	0.09
1-11	1089	5	48.69	4.56	10.49	19.12	0.27	3.67	8.80	1.94	0.89	0.89	2.24	0.255	0.59	0.13	0.16	0.27	0.07	0.14	0.09	0.09	0.05	0.04
FG1-Bc																								
EG-5	1201	6	48.94	2.00	14.43	12.50	0.16	7.58	12.17	2.06	0.27	0.14	2.36	0.519	0.25	0.08	0.17	0.23	0.06	0.04	0.18	0.04	0.02	0.04
EG-1	1161	6	47.67	3.01	12.47	14.51	0.25	5.81	10.65	2.26	0.45	0.30	2.56	0.416	0.32	0.10	0.14	0.26	0.09	0.10	0.17	0.07	0.04	0.14
EG-3	1116	6	47.88	4.59	11.14	17.52	0.29	4.20	9.33	2.11	0.75	0.58	2.41	0.299	0.33	0.16	0.13	0.16	0.08	0.06	0.15	0.11	0.06	0.09

*FG*1-*Cm*																							
1-13	1173	6	47.66	2.87	13.74	15.25	0.25	6.34	10.63	2.45	0.42	0.26		0.426	0.34	0.14	0.36	0.33	0.06	0.20	0.17	0.07	0.06	0.07
1-10	1163	6	47.69	2.99	13.98	15.30	0.20	6.14	10.38	2.43	0.44	0.27		0.417	0.54	0.18	0.30	0.25	0.03	0.15	0.14	0.13	0.04	0.07
1-8	1154	6	47.52	2.96	13.33	15.41	0.25	5.97	10.44	2.52	0.43	0.32		0.408	0.17	0.10	0.06	0.21	0.07	0.08	0.15	0.11	0.02	0.11
1-6	1144	7	47.68	3.10	12.94	15.87	0.23	5.81	10.44	2.37	0.45	0.35		0.395	0.17	0.12	0.09	0.26	0.07	0.04	0.10	0.06	0.01	0.10
1-4	1135	9	47.59	3.87	12.52	17.40	0.25	5.40	10.06	2.52	0.56	0.42		0.356	0.25	0.12	0.20	0.42	0.07	0.11	0.43	0.09	0.04	0.10
1-3	1126	7	46.78	4.14	12.06	18.07	0.26	5.06	9.87	2.57	0.58	0.42		0.333	0.29	0.12	0.09	0.47	0.06	0.09	0.10	0.05	0.03	0.09
1-2	1117	6	46.17	4.50	11.79	18.66	0.28	4.66	9.58	2.48	0.61	0.47		0.308	0.26	0.17	0.11	0.24	0.05	0.09	0.25	0.05	0.02	0.16
1-18	1107	5	46.97	5.13	11.07	19.49	0.32	4.37	9.77	1.99	0.63	0.71	2.19	0.286	0.41	0.19	0.18	0.35	0.04	0.09	0.23	0.05	0.08	0.18
1-7	1097	6	46.41	4.95	10.76	20.65	0.28	4.12	8.99	2.16	0.66	0.64	2.36	0.262	0.42	0.07	0.14	0.34	0.04	0.09	0.14	0.15	0.05	0.15
1-11	1089	8	47.26	4.38	10.50	21.10	0.26	3.53	8.65	2.17	0.87	1.16	2.37	0.230	0.42	0.15	0.11	0.45	0.07	0.08	0.24	0.08	0.03	0.20
1-12	1078	10	50.12	3.65	10.89	19.14	0.26	3.02	7.99	2.33	1.21	1.28		0.220	0.34	0.15	0.16	0.62	0.06	0.07	0.27	0.07	0.07	0.28
FG1-Cc																								
EG-4	1179	11	49.42	2.87	13.77	13.45	0.19	6.71	10.94	2.35	0.32	0.28		0.471	0.26	0.09	0.13	0.31	0.05	0.14	0.09	0.07	0.03	0.08
EG-1	1161	6	48.37	3.00	13.01	14.03	0.21	6.27	10.52	2.37	0.35	0.28		0.443	0.20	0.09	0.17	0.21	0.05	0.07	0.23	0.11	0.03	0.04
EG-2	1138	7	47.47	4.21	11.84	15.84	0.23	5.19	9.88	2.36	0.44	0.42	2.46	0.369	0.29	0.11	0.11	0.39	0.05	0.08	0.13	0.09	0.02	0.11
EG-3	1116	9	47.25	5.69	10.82	18.42	0.28	4.40	9.69	2.30	0.56	0.66	2.50	0.300	0.48	0.13	0.15	0.36	0.05	0.10	0.23	0.08	0.04	0.14
*FG*1-*Dc*																								
1-8	1154	6	48.03	4.12	12.70	15.62	0.30	5.80	9.34	2.81	0.48	0.55		0.398	0.22	0.11	0.17	0.12	0.11	0.11	0.12	0.39	0.03	0.12
1-6	1144	6	47.78	4.03	12.86	15.06	0.21	5.42	9.30	2.65	0.49	0.54		0.391	0.23	0.14	0.05	0.43	0.07	0.06	0.09	0.15	0.04	0.13
1-4	1135	7	48.13	4.42	12.58	15.81	0.24	5.41	9.40	2.59	0.54	0.53		0.379	0.27	0.20	0.18	0.28	0.11	0.14	0.17	0.07	0.03	0.11
1-3	1126	6	48.15	4.71	12.11	16.20	0.18	5.05	9.36	2.61	0.57	0.60		0.357	0.52	0.18	0.13	0.49	0.04	0.11	0.11	0.13	0.05	0.13
1-2	1117	6	48.18	5.20	11.56	16.64	0.22	4.78	9.40	2.54	0.58	0.56	2.64	0.339	0.19	0.15	0.09	0.19	0.11	0.12	0.21	0.07	0.03	0.13
1-1	1106	8	48.45	5.17	11.33	16.91	0.28	4.49	9.02	2.55	0.67	0.59	2.65	0.321	0.40	0.10	0.14	0.41	0.08	0.03	0.16	0.07	0.05	0.12
1-7	1097	6	47.79	4.92	10.49	19.50	0.27	4.09	9.04	2.16	0.69	0.92	2.56	0.272	0.74	0.15	0.20	0.53	0.04	0.07	0.17	0.12	0.04	0.18
1-11	1089	4	48.73	4.22	10.76	18.58	0.30	3.75	8.82	1.88	0.76	1.26	2.38	0.265	0.29	0.08	0.07	0.63	0.06	0.04	0.12	0.04	0.07	0.08
1-12	1078	5	50.67	3.99	10.80	18.68	0.28	3.26	8.53	1.91	1.01	1.27	2.21	0.237	0.31	0.16	0.07	0.19	0.10	0.29	0.09	0.09	0.07	0.16
FG1-Dc																								
EG-4	1179	11	48.78	4.33	12.99	14.91	0.22	5.94	9.38	2.39	0.50	0.34		0.415	0.14	0.05	0.13	0.24	0.06	0.08	0.08	0.09	0.03	0.07
EG-2	1138	7	48.60	4.39	12.01	16.87	0.25	5.08	9.76	2.48	0.59	0.36	2.68	0.349	0.82	0.21	0.14	0.57	0.07	0.08	0.29	0.12	0.06	0.05
EG-3	1116	5	48.09	5.46	11.29	16.56	0.22	4.44	9.20	2.34	0.65	0.63	2.54	0.323	0.07	0.11	0.08	0.28	0.08	0.03	0.12	0.08	0.02	0.12

FeO* is all iron given as FeO.

Mg# is the Mg/(Mg+Fe) ratio with all iron as FeO.

The corrected Na_2O values are based on the losses from Table 2.

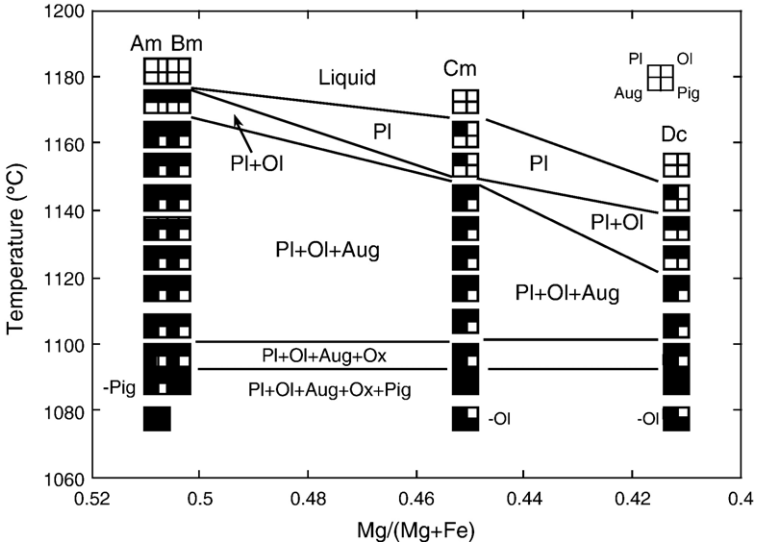

Fig. 4. Schematic representations of melting relations (Table 2) for the four samples melted at the fayalite-magnetite-quartz oxygen buffer (FMQ) as a function of melting temperature (T °C) and Mg/(Mg+Fe^{total}) of starting composition. Pl, plagioclase; Ol, olivine; Aug, augite, Ox, ilmenite and/or titanomagnetite; Pig, pigeonite. Prefix '−' indicates that the particular phase is not present.

TiO_2 contents, but after Fe–Ti oxide saturation SiO_2 increases markedly while FeO and TiO_2 decrease (Fig. 8). The calculated Fe^{3+}/Fe^{2+} ratios are relatively constant between 0.08 and 0.09 for the FMQ and between 0.050 and 0.055 for the FMQ-1 experiments. Both FeO and TiO_2 are strongly enriched with decreasing MgO until Fe–Ti oxides saturation and, thereafter, consequently markedly fall. The TiO_2 concentration decreases immediately after the appearance of Fe–Ti oxide minerals. The FeO content reaches a maximum well after the appearance of Fe–Ti oxide minerals (Fig. 8).

Although the four dike samples show generally similar liquid trends, in detail there are marked differences (Figs. 7 and 8). Of particular note, compositions *Am* and *Bm* show near constant SiO_2 with decreasing MgO, while *Cm* shows a marked decrease in SiO_2 until the appearance of Fe–Ti oxide minerals. Similarly, the FeO and TiO_2 contents reach higher values for the *Cm* sample compared to *Am* and *Bm*.

The present experimental glasses provide good constraints on the olivine, plagioclase, and augite

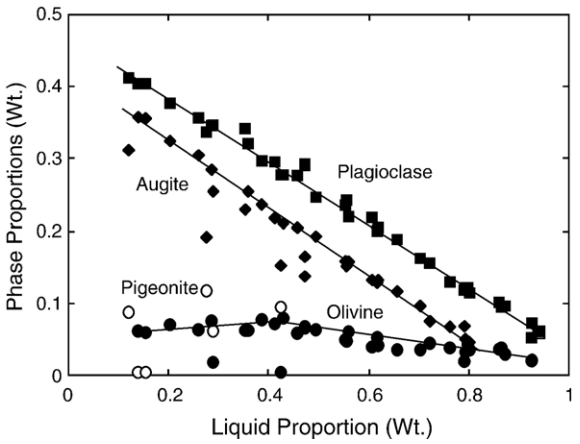

Fig. 5. Phase proportions (wt.) versus liquid proportions for all experiments at FMQ (Table 2). The proportions have been fitted to the best linear curves. Unfilled symbol is pigeonite.

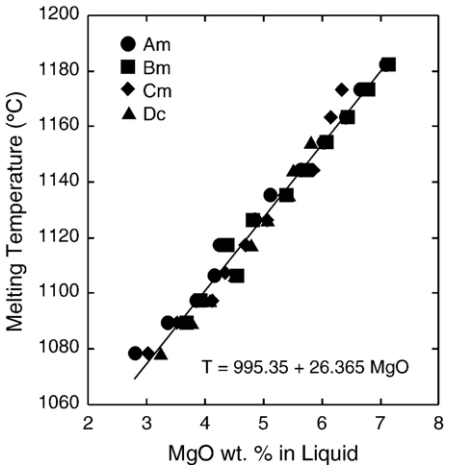

Fig. 6. Melting temperature (°C) as a function of MgO content of liquid (wt.%). The results are fitted by the linear equation T (°C)=995.35+26.365 MgO (wt.%), $\sum R^2$=0.989.

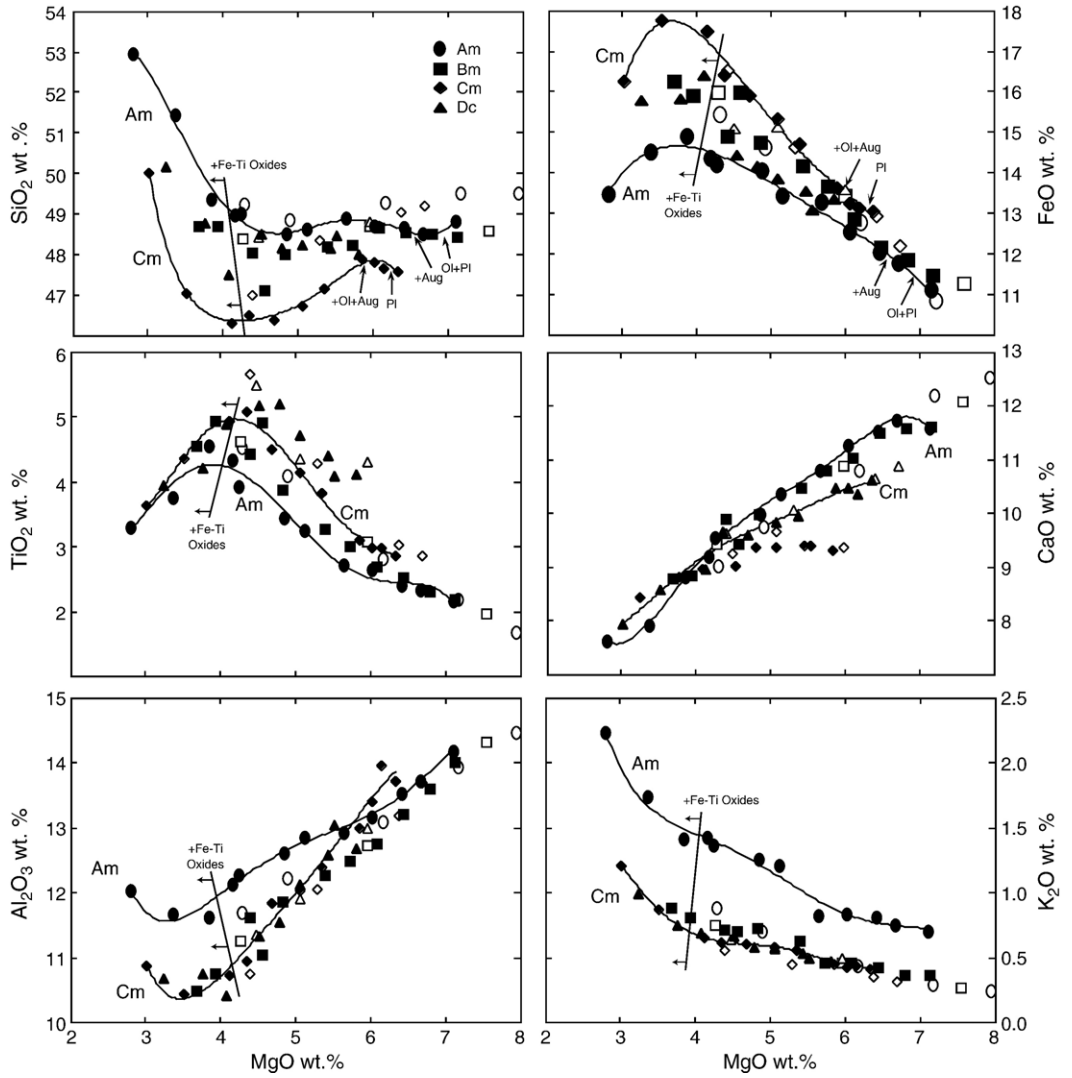

Fig. 7. Compositional variation in the liquids of all experiments as wt.% oxides. Filled symbols refer to the experiments controlled by the FMQ oxygen buffer, the unfilled symbols refer to the experiments controlled at one log unit below FMQ. Iron has been distributed between Fe^{2+} and Fe^{3+} following Kilinc et al. (1983), but only FeO is shown (see Fig. 8 for total FeO). The oxides have been normalized to 100%. Curves are fitted to the liquid lines of descent for dikes *Am* and *Cm*. Solid line marks the incoming of Fe–Ti oxide minerals. The relative incoming of olivine (Ol), plagioclase (Pl), and augite (Aug) are additionally indicated on the SiO_2 and FeO diagrams.

multiply saturated cotectic (43 experiments). This is illustrated by a projection of the glasses from olivine or quartz onto the plane orthopyroxene-wollastonite-plagioclase (Fig. 9) of the natural basalt tetrahedron using the algorithms of Longhi (1991). The results narrowly define the cotectic between 1168 °C and 1093 °C. As pigeonite appears at temperatures below 1093 °C and olivine disappears below 1084 °C, the results in addition provide preliminary constraints on the pseudoinvariant olivine, plagioclase, augite, and pigeonite and the pseudounivariant plagioclase, augite, and pigeonite cotectics. The results shown in Fig. 9 illustrate that each of the investigated samples are controlled by multiply saturated cotectics and that the liquids evolve toward increasing normative orthopyroxene (and quartz), consistent with phase relations in other equivalent low pressure studies (Walker et al., 1979; Baker and Eggler, 1987; Grove and Juster, 1989; Juster et al., 1989; Longhi, 1991; Thy and Lofgren, 1992; Snyder et al., 1993; Thy and Lofgren, 1994). The melting results also show that the starting materials (or Skaergaard dikes) are not petrogenetically related by cotectic crystallization in volatile-free system under atmospheric conditions (cf., Fig. 8).

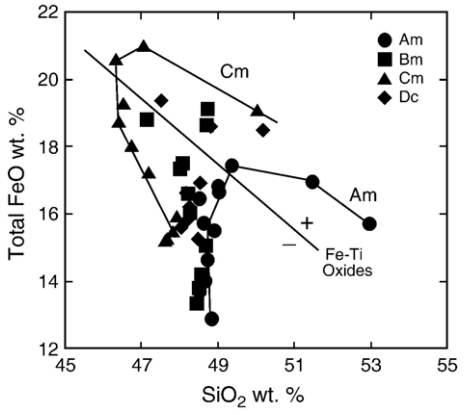

Fig. 8. Total FeO versus SiO_2 content of glasses in wt.%. Data and calculation as for Fig. 7. The income of Fe–Ti oxide minerals is indicated.

Olivine ranges in composition from Fo_{80} to Fo_{51} and is well correlated with melting temperature and compositional variables (Supplementary Dataset 1 (Table 4)). The distribution coefficient for Mg and Fe^{2+} between olivine and liquid ($K_D^{FeO/MgO}$ (ol/liq)= $(X_{FeO}/X_{MgO})^{ol}/(X_{FeO}/X_{MgO})^{liq}$ in moles) is 0.334±0.013 for the FMQ-1 experiments (13 determinations) and 0.326±0.016 for the FMQ experiments (33 determinations) (±1 standard deviation). The average K_D for all experiments is 0.328±0.016 (Fig. 10A). This K_D is relatively high compared to typical values based on basaltic compositions (Roeder and Emslie, 1970; Ussler and Glazner, 1989; Ulmer, 1989), but not unlike other determinations on ferrobasaltic compositions (Hoover and Irvine, 1977; Toplis and Carroll, 1995). The distribution of Fe^{2+} and Mg between olivine and liquid is weakly dependent on f_{O_2} (Roeder and Emslie, 1970; Kilinc et al., 1983; Ulmer, 1989; Snyder and Carmichael, 1992). The K_D may also be dependent on very iron rich and silica undersaturated systems because of non-ideal mixing (Hoover and Irvine, 1977; Gee and Sack, 1988; Toplis and Carroll, 1995; Toplis, 2005) resulting in a marked increase in K_D for ferrobasaltic compositions. However, only weak negative correlation has been found between K_D and melting temperature in this study. The uniform K_D values obtained for the Mg–Fe exchange between olivine and liquid (Fig. 10A), as well as absolute values, demonstrate a high degree of equilibration (cf., Toplis, 2005).

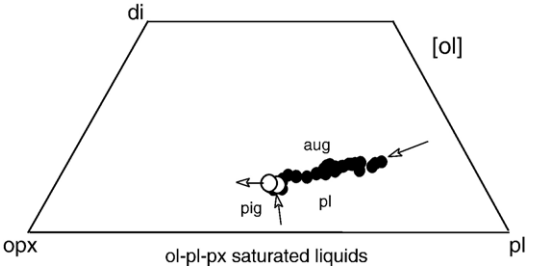

Fig. 9. Experimental liquids projected from olivine onto the triangle opx-wo-pl in oxygen units (Longhi, 1991). Abbreviations are di, diopside; ol, olivine; pl, plagioclase; opx, orthopyroxene; aug, augite; and pig, pigeonite. Filled symbols represent liquids saturated in olivine, plagioclase, and augite. Unfilled symbols represent liquids in addition saturated in pigeonite (*Cm* only).

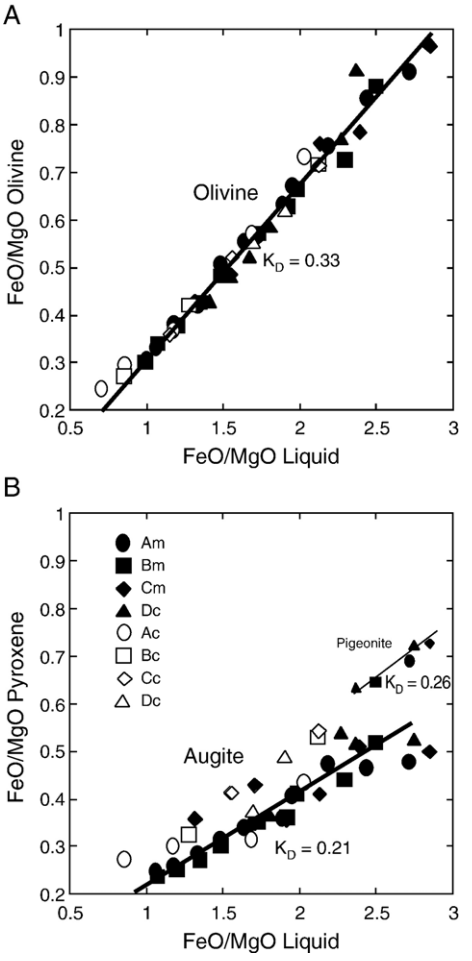

Fig. 10. FeO/MgO for olivine (A) and pyroxenes (augite and pigeonite) (B) versus FeO/MgO for coexisting liquid (mole proportions). The Fe^{3+}/Fe^{2+} ratio of the liquid was calculated after Kilinc et al. (1983). For olivine, all iron was calculated as Fe^{2+}. The Fe^{3+}/Fe^{2+} of augite was kept constant (see text). For pigeonite, all iron for both mineral and liquid was calculated as Fe^{2+}. The melting experiments controlled by the FMQ oxygen buffer resulted in K_D for olivine of 0.330±0.014, for pigeonite 0.262±0.005, and for augite 0.211±0.022 (±1 standard deviation). Filled symbols refer to the experiments controlled by the FMQ oxygen buffer, the unfilled symbols refer to the experiments controlled one log unit below FMQ.

Plagioclase ranges in composition from An_{79} to An_{49}, but shows only poorly defined correlation between composition and melting temperature (Supplementary Dataset 2 (Table 5)). The exchange of Na and Ca between plagioclase and liquid defined as Na_2O/CaO (pl/liq)$=(X_{Na2O}/X_{CaO})^{pl}/(X_{Na2O}/X_{CaO})^{liq}$ is about 1.40 with a weak negative correlation between K_D and melting temperature. This is consistent with other experimental results on a large variety of basalt compositions (Grove and Baker, 1984; Thy, 1992; Toplis and Carroll, 1995; Thy et al., 1998, 1999). The high uncertainty in the composition of plagioclase (Supplementary Dataset 2 (Table 5)) that for some low temperature experiments reaches 5 mol% An is attributed to the difficulty of attaining equilibrium.

Augite shows wide compositional variation from $En_{48}Fs_{10}Wo_{42}$ to $En_{39}Fs_{26}Wo_{35}$ (Fig. 11) and depends strongly on temperature (Supplementary Dataset 3 (Table 6)). In order to evaluate the exchange of Fe^{2+} and Mg between augite and liquid, the Fe_2O_3 contents of the augites were estimated by charge balancing cations (Papike et al., 1974). This analysis shows an average Fe^{3+} content of about 0.03 per formula unit, corresponding to an average Fe_2O_3/FeO ratio of 0.22. Based on this recalculated FeO content, an average K_D for the exchange of Fe^{2+} and Mg between augite and liquid of 0.211 ± 0.022 is calculated (Fig. 10B). In addition, there is a small but significant positive correlation between melting temperature and K_D that for sample Am is adequately described by the equation $K_D=0.771-630.12/T$ (°C) ($\sum R^2=0.816$). These results are similar to those obtained by Thy et al. (1998) for relatively magnesian lavas from ODP Leg 152 and by Hoover and Irvine (1977) for an Fe_2O_3-free system. Because of the small temperature dependencies of the K_D's for olivine/liquid and pyroxene/liquid, the distribution coefficient for Mg and Fe^{2+} between coexisting olivine and augite ($K_D^{FeO/MgO}$ (ol/px)) varies from 1.4 to 1.9 and is negatively correlated with temperature.

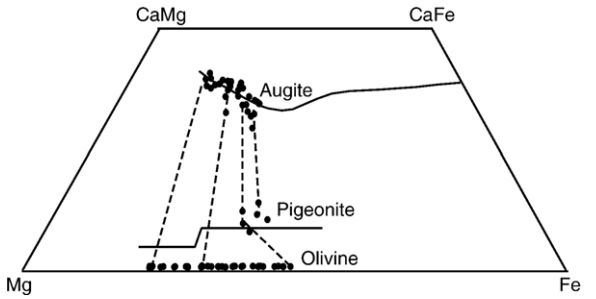

Fig. 11. Mg–Ca–Fe relations for the experimental olivine and pyroxenes. Representative tie-lines are between typical coexisting augite and olivine, augite and pigeonite, and pigeonite and olivine. All iron is calculated as Fe^{2+}. The Skaergaard trend for high-Ca and low-Ca pyroxenes is shown for comparison (Brown and Vincent, 1963).

Pigeonite ranges in composition from $En_{54}Fs_{38}Wo_8$ to $En_{51}Fs_{37}Wo_{12}$ (Fig. 11; (Supplementary Dataset 3 (Table 6)). Assuming that all iron in pigeonite occurs as Fe^{2+}, the Fe^{2+} and Mg exchange coefficient for the pigeonite-liquid pairs ($K_D^{FeO/MgO}$(pig/liq)), obtained within a narrow temperature interval of 1089–1078 °C, is 0.262 ± 0.005 (Fig. 10B).

For the majority of the melted samples, ilmenite is the first Fe–Ti oxide mineral and is followed shortly by titanomagnetite (Table 2 and Supplementary Dataset 4 (Table 7)). Assuming perfect stoichiometry, ilmenite contains an average of 8.6 mol% hematite and the coexisting titanomagnetite contains 24.2 mol% ulvöspinel. The coexisting Fe–Ti oxide pairs indicate an equilibrium temperature of 1091 °C and a f_{O_2} of 10–10.07 (Buddington and Lindsley, 1964; Andersen and Lindsley, 1988). These values correspond well with the experimental melting temperatures of 1097–1078 °C and f_{O_2} of $10^{-9.95}$–$10^{-10.10}$ (for the FMQ oxygen buffer). Ilmenite equilibrated at one log-unit below FMQ contains significantly lower hematite contents (3.9%), showing that the experimental products were well equilibrated with the furnace gas.

4.4. Instantaneous solid modes

The systematic modal variation allows us to model (1) the experimental equilibrium solid modes and (2) the instantaneous solid modes along the pertinent cotectics. The instantaneous solid modes are equal to the slope of the equilibrium modes as a function of liquid fraction (Fig. 5). Because the equilibrium modes are approximated by linear relationships, the instantaneous modes can be modeled as constants (see Appendix). Incorporating results of Thy and Lofgren (1992, 1994) and Toplis and Carroll (1995), the instantaneous modes for the plagioclase-olivine cotectic are approximated by 0.264 olivine and 0.736 plagioclase (as total solids in weight fractions). The cotectic proportions along the olivine-plagioclase-augite cotectic are particularly well constrained by the present data and yield instantaneous modes of 0.092 ± 0.011 olivine, 0.463 ± 0.010 plagioclase, and 0.446 ± 0.010 augite (±standard error). These proportions can be compared to the results of Toplis and Carroll (1995) that, for a slightly more aluminous starting composition (Table 1, SC1), gave 0.12 olivine, 0.48 plagioclase, and 0.40 augite along the same multiply saturated cotectic.

The instantaneous modes for olivine are less well constrained than for the other silicates and several possibilities exist for fitting the low temperature results (Fig. 4). The slope (0.09) obtained for the relatively high temperature range does not fit the data well for the low temperature range. A linear fit to the full data set results in a significantly lower slope (~0.05) and consequently smaller instantaneous modes for olivine that fail to produce decreasing liquid MgO content even at relatively high liquid fractions. However, a change in the slope of the olivine curve may occur with the appearance of pigeonite at a liquid fraction of about 0.40. As discussed above, this presumably signals the termination of olivine crystallization and a reaction relationship between liquid and olivine. Toplis and Carroll (1995) noted a significant modal decrease in olivine abundance below about 1100 °C (FMQ) and related this to resorption of olivine during magnetite crystallization (low-Ca pyroxenes were not detected). The present results show that resorption of olivine is related to crystallization of pigeonite and not magnetite.

The instantaneous modes for ilmenite and magnetite are poorly constrained as functions of melt content and oxygen fugacity. Incorporating results from Thy and Lofgren (1994) on ferrobasalts suggest modes of 0.138 ilmenite and 0.072 magnetite for the FMQ buffer. Calculation of fractional crystallization using these modes often results in a rapid drop in TiO_2 content to the extent that Ti-bearing minerals no longer can be in equilibrium with the coexisting liquid (cf., Toplis and Carroll, 1995, p. 1160). Consideration of other experimental data (Juster et al., 1989; Snyder et al., 1993) still does not offer better constraints on the instantaneous modes past the appearance of Fe–Ti oxide minerals. It is plausible, but not experimentally constrained, that the modes of Fe–Ti oxides decrease as iron and titanium are depleted in the liquid. The calculations of Toplis and Carroll (1996) assume that the amount of ilmenite is constant and that magnetite was the dominating Fe–Ti oxide. Toplis and Carroll (1996) further were unable directly to use their experimentally determined modes of magnetite and instead calculated these by mass balance as a function of temperature and f_{O_2}. This contrasts to the present study that applies the experimental results suggesting that ilmenite is dominating and indicates ilmenite and magnetite modes much lower than suggested by Toplis and Carroll (1996). The Fe–Ti oxide modes preferred in this study assume a systematic decrease in ilmenite as a function of temperature and a constant, but small, content of magnetite.

Fe–Ti oxide modes are known to be dependent on f_{O_2} (Snyder et al., 1993; Toplis and Carroll, 1995). Despite this, there only exist data for redox conditions near the FMQ buffer (FMQ ± 1) and temperatures above 1060 °C (Snyder et al., 1993; Thy and Lofgren, 1994; Toplis and Carroll, 1995). For redox conditions markedly deviating from the FMQ oxygen buffer and for temperatures below 1060 °C, few reliable data exist on Fe–Ti oxide-silicate and Fe–Ti oxide-silicate-phosphate phase relations. The uncertainties in the extrapolation of experimental results to very low temperatures and for extreme redox conditions are thus associated with considerable uncertainty. We will in this paper demonstrate that the limitations in our understanding on the effect of f_{O_2} are not a serious problem for understanding Skaergaard. Further, we will terminate all the model calculations in the UZ at temperatures of 1000 °C, above the inferred crystallization temperatures for SH (980–950 °C, Lindsley et al., 1969).

4.5. Quantitative crystallization models

The experimental conditions used in this study approximate equilibrium crystallization in a system open to oxygen. A consequence is that the experimental results are not directly applicable to the Skaergaard intrusion that predominantly was controlled by crystal fractionation and redox conditions that may have been closed with respect to exchange of oxygen. In order to predict the evolution of Skaergaard parental melts and related magmas, we have developed a crystallization model based on the present experimental results (Appendix). The model calculations allow the compositions of coexisting liquid and minerals to be calculated with decreasing liquid fraction remaining as a function of redox conditions. We have in this study obtained experimental results directly applicable to Skaergaard related magma compositions and base the modeling principally on these results. Other existing generalized crystallization models (e.g., Nielsen, 1988; Weaver and Langmuir, 1990; Longhi, 1991; Ghiorso and Sack, 1995; Ariskin, 1999) are not directly applicable to the specific evolved ferrobasaltic magma compositions of the Skaergaard intrusion.

The crystallization model employs mass balance calculations for each oxide (SiO_2, TiO_2, Al_2O_3, Fe_2O_3, FeO, MnO, MgO, CaO, Na_2O, K_2O, P_2O_5) as a function of the solid fraction incrementally going from 0 to 1 in small and constant steps of the liquid remaining. The temperature for each increment is estimated from its linear relationship with liquid MgO content (Fig. 6; Appendix A). The compositions of the stable phase assemblage in equilibrium with the coexisting liquids

are determined from experimentally simple and compound exchange coefficients, either as constants or as linear functions of temperature (see Appendix A). In addition, stoichiometric constraints have been imposed on all silicate minerals. Thus, the calculated equilibrium mineral compositions at each increment are by definition in equilibrium with the coexisting liquid at the specific temperature.

The composition of the equilibrium (M_s) and instantaneous (M_s^*) bulk solids can easily be calculated from the experimentally determined modes and mineral compositions. Using this information, equilibrium crystallization can be modeled by solving the mass balance equation

$$M_o = (1 - F) \times M_l + F \times M_s \quad (1)$$

for the liquid composition (M_l) over a range of F, where F is the solid fraction and M_o is the constant starting composition.

Similarly, fractional crystallization can be modeled by solving the mass balance equation

$$M_o^* = (1 - i) \times M_l^* + i \times M_s^* \quad (2)$$

sequentially for the liquid composition (M_l^*), where i is the crystallization increment and M_o^* is the previously determined liquid composition. This modeling approximates perfect fractional crystallization for $i \rightarrow 0$. Therefore, the approximation to perfect fractional crystallization is determined by the size of the increment. The effect of increment size is illustrated by calculations done for a range of fractionation steps. For $i = 0.01$, corresponding typically to a drop in liquid temperature of about 1 °C, the modeled olivine composition is $Fo_{45.2}$ at a liquid fraction remaining of 0.5. Decreasing the increments to $i = 0.0001$ yields an olivine composition of $Fo_{46.2}$ at an identical liquid fraction. Even smaller increments will produce closer approximations to perfect fractional crystallization, but will not significantly affect the modeling even for relatively small amounts of liquid remaining.

The availability of oxygen for iron oxidation is modeled for two different conditions. For systems open to oxygen, the liquid at each crystallization increment is adjusted along the chosen oxygen buffer curve using the equations of Kilinc et al. (1983). Systems closed to oxygen are initially constrained by adjusting the Fe^{3+}/Fe^{2+} of the starting composition to the selected oxygen buffer. Because Fe^{3+} is partitioned into augite, ilmenite, and magnetite, f_{O_2} will vary as a function of liquid fraction as well as crystallization temperature.

5. Exploratory modeling of Skaergaard liquids

In this section, we explore the effects of equilibrium or fractional crystallization, conditions open or closed to oxygen, variations in oxygen pressure, fractionating solid modes, and crystallization temperatures and orders on the liquid line of descent of the Skaergaard intrusion. We will examine the effects on the liquid evolution path, principally with respects to the iron and silica variations. We use a Skaergaard dike as the starting composition for the majority of the calculations (Table 3, analysis *Cm*, 1–13). Except as otherwise specified, all modeling was done for conditions open with respect to exchange of oxygen and for fractional crystallization. The insight gained is used as a first order guide for discussing the Skaergaard liquid line of descent.

5.1. Equilibrium versus fractional crystallization

Although it is often assumed that fractional crystallization is dominating, magmatic processes are, irrespectively of the actual mode of fractionation (gravitative or in-situ segregation), likely to record components of equilibrium crystallization resulting from partial reequilibration of phenocrysts and the failure of removal or isolation of mineral grains. The evolution of magmatic systems during equilibrium crystallization thus has more than theoretical petrogenetic interest. An additional interest is that equilibrium crystallization provides a first order test of the formulated forward crystallization model by its ability to duplicate the experimental results.

Fig. 12 illustrates the principal differences between the two end-member differentiation modes also documented by others (Langmuir and Hanson, 1981; Ghiorso and Carmichael, 1985, 1987; Toplis and Carroll, 1996; Ghiorso, 1997). The calculations are done with a small initial interval of olivine and plagioclase crystallization prior to the appearance of augite ($F = 0.11$; Fig. 5), as observed in the layered series, and are terminated at the point when Fe–Ti oxide minerals join the crystallizing assemblage ($F = 0.40$–0.50, ~1100 °C; Table 2). The results demonstrate a reasonable correspondence between the experiments and the modeling of equilibrium crystallization and confirm that the numerical modeling approach can reproduce main features of the experimental results.

Equilibrium crystallization yields a slightly higher solid fraction ($F = 0.50$) than fractional crystallization ($F = 0.40$) at similar model temperature (1100 °C) (Fig. 12B). The liquid compositions are relatively depleted in SiO_2, FeO, and Na_2O and enriched in TiO_2 for

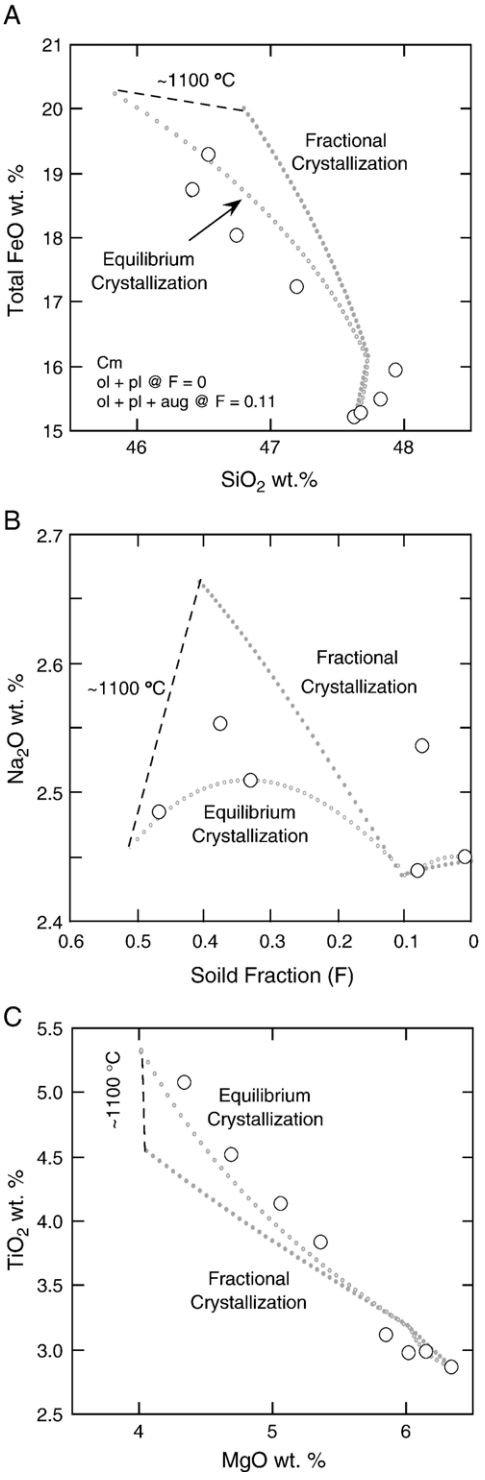

Fig. 12. Fractional versus equilibrium crystallization for conditions open with respect to oxygen and referenced to the FMQ oxygen buffer. The modeling assumes olivine and plagioclase at 1164 °C, augite at 1154 °C, and is terminated at 1100 °C. Circles are the experimental glasses for *Cm* (Table 3). (A) Total FeO versus SiO_2 (wt.%). (B) Na_2O versus solid fraction (*F*). (C) TiO_2 versus MgO (wt.%).

equilibrium compared to fractional crystallization, at similar MgO content or solid fraction (*F*) (Fig. 12). This is the result of preferential removal of relatively forsteritic olivine and anorthitic plagioclase that leads to enrichments in FeO and Na_2O in liquids from perfect fractional crystallization. This will principally be manifested in relatively anorthitic plagioclase and forsteritic olivine for conditions involving a large component of equilibrium crystallization (Toplis and Carroll, 1996; Ghiorso, 1997).

Components of equilibrium crystallization have been proposed for the Skaergaard intrusion. Ariskin (1999) has suggested that Skaergaard fractionation was controlled by crystal-melt equilibrium intermediate between equilibrium and fractional crystallization in crystal-rich parental melt. It has also been pointed out that the apparent restricted evolution in plagioclase compositions compared to olivine observed for the late stage Skaergaard cumulates may record a component of restricted fractional crystallization of plagioclase (Maaløe, 1976a,b). This may be caused by the inability of plagioclase to sink in Skaergaard melts (Campbell et al., 1978), leading to the coexistence of relatively calcic plagioclase (An_{30}) with iron-rich olivine (Fo_0) in the final solid products.

5.2. Oxygen fugacity

Oxygen fugacity (f_{O_2}) strongly affects magmatic differentiation products (Hamilton et al., 1964; Biggar, 1974; Hill and Roeder, 1974). The f_{O_2} influence the saturation of Fe–Ti oxide minerals, solid and liquid Fe^{3+}/Fe^{2+} ratios, mineral assemblages and modes, and ultimately the liquid line of descent (Juster et al., 1989; Grove and Juster, 1989; Snyder et al., 1993; Ariskin and Barmina, 1999; Ariskin, 1999, 2002).

The crystallization conditions of UZc were estimated by Lindsley et al. (1969) from Fe–Ti oxide-silicate mineral equilibria (600±100 bar; 980–950 °C; $f_{O_2}=10^{-13}$–$10^{-13.6}$ atm). Williams (1971) extended the f_{O_2} estimates to the full depth of the LS, calculating an f_{O_2} near, and approximately parallel to, the FMQ oxygen buffer for LZ and MZ, and with a marked drop to near the MW oxygen buffer for UZc (see also Frost et al., 1988). Similar studies have suggested that f_{O_2} decreases systematically from near FMQ in the LZc to the magnetite-wüstite (MW) oxygen buffer in the UZc (Morse et al., 1980; Morse, 1990; Frost and Lindsley, 1992). Such low f_{O_2} has been confirmed by Larsen et al. (1992) in a study of methane-bearing late magmatic fluids trapped as inclusions in interstitial apatite, feldspars, and quartz in the upper MZ and the UZ.

It was demonstrated by Toplis and Carroll (1995) that the appearance of magnetite is positively dependent on f_{O_2} (24 °C/log f_{O_2} unit). For conditions below FMQ+1 (one log-units above FMQ), the appearance of ilmenite is largely independent of f_{O_2} (Toplis and Carroll, 1995). Near the FMQ buffer, the two oxide minerals appear nearly simultaneously at about 1100 °C (Thy and Lofgren, 1994; Toplis and Carroll, 1995; Ariskin and Barmina, 1999). Reduced conditions thus may delay saturation of titanomagnetite and consequently result in iron enrichment in the melt (Fig. 13). This is understandable since titanomagnetite saturation in part depends on Fe_2O_3 concentration of the liquid (Ariskin and Barmina, 1999).

Fig. 13 illustrates the effect of changes in the relative income of augite and Fe–Ti oxides. The curves are calculated based on the T–f_{O_2} phase diagram determined by Toplis and Carroll (1995) and the Fe–Ti oxide modes for the FMQ oxygen buffer. The modeling thus takes into consideration the f_{O_2} effects on Fe–Ti oxide crystallization and composition, but does not incorporate the effect of f_{O_2} on modes and uses constant TiO_2 content of oxides (Appendix).

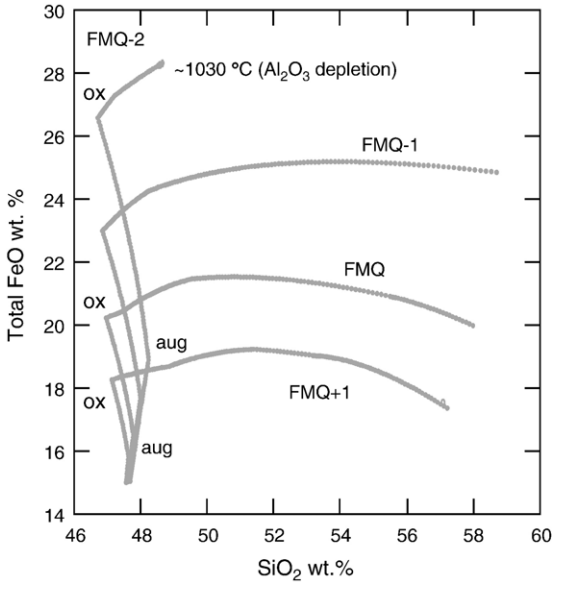

Fig. 13. The effects of f_{O_2} on fractional crystallization open with respect to oxygen. The modeling assumes olivine and plagioclase at 1164 °C, augite at 1149 °C, Fe–Ti oxides at 1102 °C, pigeonite replacing olivine at 1093 °C, olivine replacing pigeonite at 1046 °C, and terminated at 1000 °C. The effects on the crystallization temperatures of augite (~7 °C/log unit) and Fe–Ti oxides (~24 °C/log unit) are from Toplis and Carroll (1995). For FMQ-2, the suppression of oxide crystallization causes depletion in Al_2O_3 at about 1030 °C. Abbreviations: ox, Fe–Ti oxides; aug, augite.

Nevertheless, the calculations predict that maximum iron content increases with decreasing f_{O_2} principally as a result of suppression of magnetite crystallization. It is further shown that modest iron enrichment continues into MZ, together with strong silica enrichment, well past Fe–Ti oxide saturation. For conditions at, or below, FMQ-2, the liquid may become depleted in Al_2O_3 at a relatively early stage and hence unable to crystallize feldspar (~1030 °C for FMQ-2) because of prolonged formation of feldspar-rich rocks (anorthosite, troctolite, or gabbro). This points to the critical importance of f_{O_2} and Fe–Ti oxide mineral fractionation in producing late feldspar-rich differentiates, like in the Skaergaard intrusion.

5.3. Conditions open or closed to oxygen

Fractional crystallization under conditions of externally buffered oxygen (open with respect to oxygen) constrains the Fe^{3+}/Fe^{2+} ratio of the melt and results in an externally controlled f_{O_2}. In contrast, crystallization under a constant oxygen content (closed with respect to oxygen) results in a liquid path of variable f_{O_2} controlled by the crystallizing mineral phases and their Fe^{3+} contents. In order to model crystallization with constant oxygen, Fe^{3+} is treated as an included element in magnetite, ilmenite and augite and f_{O_2} is calculated from the liquid Fe^{3+}/Fe^{2+} ratio and the crystallization temperature (Kilinc et al., 1983).

During fractional crystallization closed with respect to oxygen, f_{O_2} will initially increase (Fig. 14) causing a slightly earlier appearance of both augite and titanomagnetite, compared to crystallization open with respect to oxygen. With the appearance of augite, the rise in f_{O_2} is markedly dampened by the incorporation of Fe^{3+} into augite. After the appearance of Fe–Ti oxide minerals, the Fe^{3+}/Fe^{2+} ratio of the liquid and f_{O_2} decrease. The magnitude of this f_{O_2} decrease is strongly dependent on the amount of crystallizing Fe–Ti oxides, as well as on the ilmenite/magnetite ratio of the solid fractionates.

The first set of model calculations illustrated in Fig. 14 uses the Fe–Ti oxide modes obtained in this study for FMQ (mt/il=0.5; Appendix A). The results suggest a modest UZ drop in f_{O_2} and little differences in the FeO–SiO_2 relations for the two basic treatments of oxygen after the appearance of Fe–Ti oxides. The principal effect of decreasing f_{O_2} is suppression in magnetite crystallization (cf., Osborn, 1959; Toplis and Carroll, 1995) that may delay iron depletion and silica enrichment in the melt (Fig. 13). It, nevertheless, can be anticipated that the difference in Fe–Ti oxide modes

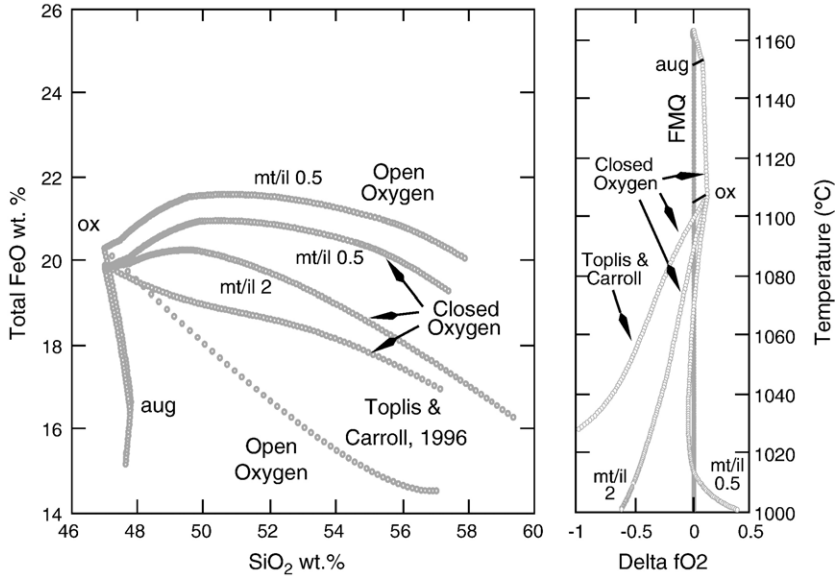

Fig. 14. Fractional crystallization open or closed with respect to oxygen and referenced to the FMQ oxygen buffer. The crystallization orders used in the calculations are similar to those used in Fig. 13. Because of increasing f_{O_2}, closed system crystallization results in earlier appearance of augite (2 °C) and Fe–Ti oxides (4 °C) compared with crystallization open with respect to oxygen. Because of the lack of experimental data, identical Fe–Ti oxide modes are used for both open and closed system crystallizations (see discussion in text). Two models are shown based in the present experimental results: with mt/il ratio of 0.5 as experimentally determined (see Appendix A) and with the mt/il ratio arbitrarily reversed to 2. The modeling marked 'Toplis and Carroll, 1996' is based on the instantaneous Fe–Ti oxide modes calculated by Toplis and Carroll (1996), respectively, for open and closed conditions with respect to oxygen. Delta f_{O_2} is the calculated f_{O_2} minus the f_{O_2} for the reference FMQ oxygen buffer.

will be minor at the points where Fe–Ti oxides first appear on the liquidus. This is because of the relatively small ΔFMQ (~0.1 log-unit) calculated at this point between open and closed conditions with respect to oxygen (Fig. 14). This observation supports the suggestion in this study that f_{O_2} and the FeO content of the liquid only show modest variation after the start of Fe–Ti oxide crystallization.

Toplis and Carroll (1996) calculated by mass-balance significantly higher LZc modal proportions of titanomagnetite for open than for closed system conditions (approximately 42 versus 17 wt.% at 1100 °C). To these estimated magnetite modes must be added somewhat smaller, but relatively constant, ilmenite modes (~8 wt.%). These very high Fe–Ti oxide modes for both variable and constant oxygen contents conflict with the present experimental results and modeling (Fig. 14) that do not support large amounts of crystallizing Fe–Ti oxide minerals. There are three reasons for this, necessitated by the new experimental results. First, augite contains appreciable higher amounts of Fe^{3+} than in the modeling of Toplis and Carroll (1996). Secondly, the modal contents of Fe–Ti oxide minerals in the modeling are much lower than that inferred by Toplis and Carroll (1995). Thirdly, ilmenite is the dominant Fe–Ti oxide mineral in the present modeling in contrast to Toplis and Carroll (1996) who calculated magnetite to be the overwhelmingly dominant oxide mineral.

The strong variation in f_{O_2} seen in Fig. 14 is confined to the late stage evolution (UZc) and is caused by the relative depletion of Fe^{2+} and Fe^{3+}, dependent on the absolute and relative amounts of the Fe–Ti oxide minerals. The model calculation based on the present experimental results predicts UZc oxidation as a result of depletion in Fe^{2+} relative to Fe^{3+}. Other models that conform better to the UZ f_{O_2} variation predicted from mineral equilibrium calculations (e.g., Williams, 1971; Morse et al., 1980) can be formulated by increasing the modal content of magnetite in the solid fractionate. Two such examples are illustrated in Fig. 14. The first uses the modal estimates of Toplis and Carroll (1996) and predicts a strong drop in f_{O_2} and depletion in FeO with advanced crystallization (mt/il ratio vary between 2 and 0.8). The high Fe–Ti oxide modes for both variable and constant oxygen in the model based on the modes of Toplis and Carroll (1996) translate into a strong depletion in iron and predicts a significant LZc to UZ decrease in f_{O_2}, resulting from the removal of high amounts of Fe_2O_3 with the magnetite-rich solid

fractionate (Fig. 14). The other model shown in Fig. 14 arbitrarily reverses the ratio of the two oxide minerals obtained in this study (from mt/il=0.5 to mt/il=2). This latter model predicts f_{O_2} variation better in accord with expectations and also predicts FeO depletion with SiO_2 enrichment in UZ (Fig. 14).

There is good evidence in favor of crystallization of the Skaergaard magma under variable f_{O_2} and, thus, under conditions closed to the exchange of oxygen (Osborn, 1959; Presnall, 1966). Osborn (1959) showed that crystallization in quaternary systems open with respect to oxygen would result in liquid paths departing from cotectic proportions because of the constraints imposed by isobaric p_{O_2}. For example in the $MgO–SiO_2–FeO–Fe_2O_3$ system (Muan and Osborn, 1956; Osborn, 1959; Roeder and Osborn, 1966), constant p_{O_2} restricts the liquid evolution to within a subternary $MgO–SiO_2–(FeO \cdot Fe_2O_3)$ system (p_{O_2}=0.21 atm) nearly perpendicular to the dominating silicate-magnetite cotectics in the quaternary. The consequence is a relatively stronger liquid enrichment in silica and depletion in iron for systems evolving at constant p_{O_2}, mainly caused by higher modal proportions of Fe–Ti oxides (or lower silicate proportions) along the ternary cotectics. Osborn (1959, 1962) and Presnall (1966) used these experimental results to argue that the Skaergaard intrusion "represents the results of a close approach to fractional crystallization of an essentially anhydrous magma at constant total composition" (i.e., closed system; Presnall, 1966, p. 753). The finding of Toplis and Carroll (1996) is fundamentally in accord with the findings from simplified systems.

The experiments on which the present calculations are based were conducted on multicomponent ferrobasaltic liquids at conditions open to oxygen. Such experiments unequivocally yield isobaric liquid evolution paths with restricted iron enrichments (cf., Fig. 8). The experimental mineral assemblages suggest crystallization relatively well constrained by univariant cotectic relations of silicate minerals (Fig. 9), quantitatively similar to those observed in the quaternary system by Osborn (1959). It is expected that this cotectic with increasing variance, adding magnetite, may delineate a divariant surface in the quinary system and, therefore, may not be applicable for tracing crystallization involving Fe–Ti oxides under conditions of variable f_{O_2}. To achieve this, direct experimental determination of the effect of variable f_{O_2} on ferrobasaltic compositions are required.

Our experiments and model calculations suggest that the onset of Fe–Ti oxide crystallization influenced the liquid line of descent of the Skaergaard intrusion. However, we do not find support for the marked drop in liquid iron content and f_{O_2} caused by fractionation of large volumes of Fe–Ti oxides as is widely proposed (Hunter and Sparks, 1987; Toplis and Carroll, 1996). Our experimental results in contrast support fractionating Fe–Ti oxide modes consistent with petrographic observation and support modest to little iron depletion and only a small drop in f_{O_2} well into UZ. The calculations predict that the effect of crystallization under conditions closed with respect to oxygen, at least for MZ and UZa, will have only minimal effects on the liquid line of descent. There is also no support for continuing depletion in silica past Fe–Ti oxide appearance in LZc and MZ (McBirney and Naslund, 1990).

5.4. Modal proportion of solids

The Fe–Ti oxide minerals are particularly important for understanding the crystallization of the Skaergaard intrusion. Magnetite appears as an early crystallizing mineral in LZc (Wager and Deer, 1939; Wager and Brown, 1967). Ilmenite is by far the most volumetrically important Fe–Ti oxide mineral in LZc to UZc (Wager and Deer, 1939; Vincent and Phillips, 1954; McBirney, 1996; Jang and Naslund, 2003). There is some uncertainty concerning the status of ilmenite in the LZ. Wager and Deer (1939) observed that both Fe–Ti oxide minerals became abundant at the base of LZc. Later interpretations by Wager and Brown (1967) have suggested that ilmenite grains appear in the LZa and LZb and that this phase became saturated when LZa formed. However, petrographic examinations of the LZ suggest that ilmenite and magnetite occur nearly simultaneously at the base of LZc and that euhedral ilmenite grains below this horizon crystallized from an intercumulus melt (e.g., Irvine et al., 1998).

The absolute modes of Fe–Ti oxide minerals control the late stage evolution and determine whether the liquid path evolves toward increasing iron past Fe–Ti oxide crystallization. Three different and reasonable modal Fe–Ti oxide distributions are illustrated in Fig. 15 (cf., Appendix). Model C assumes constant modes of magnetite (7 wt.%) and ilmenite (14 wt.%). This model is based on the present results as well as those of Thy and Lofgren (1994) on evolved tholeiitic Icelandic ferrobasalts similar the Skaergaard dikes. The total Fe–Ti oxide mode in Model C compares reasonably to that used by Grove and Baker (1984) and Juster et al. (1989) for modeling the evolution of the

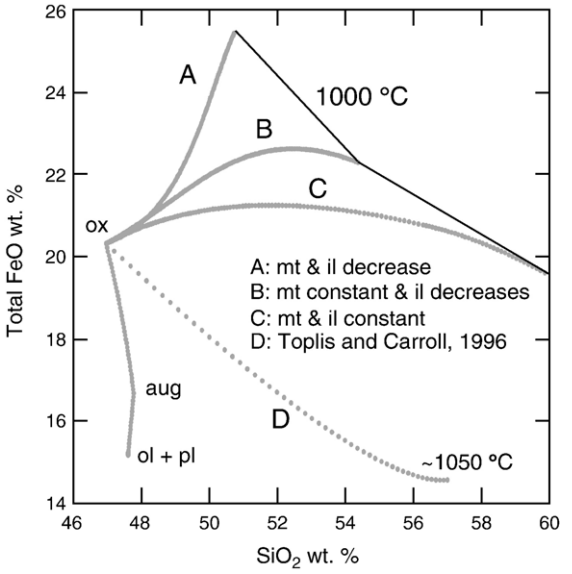

Fig. 15. The effects of variable Fe–Ti oxide mineral modes for fractional crystallization open with respect to oxygen and referenced to the FMQ oxygen buffer. The crystallization orders used in the calculations are similar to those used in Fig. 13, except that pigeonite has been excluded. The Fe–Ti oxide modes used in the calculations are given in Appendix (Models A, B, and C). Model D is based on Toplis and Carroll (1996). Abbreviations: ol, olivine; pl, plagioclase; aug, augite; ox, Fe–Ti oxides.

Galapagos ferrobasalts (15–20 wt.%, magnetite only). The modal information on LS gabbros suggests total Fe–Ti oxide contents in the range of 5–15 vol.% (cf., Wager and Deer, 1939; Vincent and Phillips, 1954; Wright, 1961; Wager and Brown, 1967; Conrad and Naslund, 1989; Sørensen, 1995).

Toplis and Carroll (1995, 1996) experimentally determined the initial modes of ilmenite as 8 wt.%, very similar to the present finding. However, Toplis and Carroll (1996) were unable experimentally to determine the magnetite mode and employed an indirect mass balance calculation method that resulted in very high initial modes of magnetite (~42 wt.%). Therefore, the modeling of Toplis and Carroll (1996) uses an initial total amount of Fe–Ti oxides above 50 wt.% that is inconsistent with other experiments and petrographic studies of the Skaergaard cumulates. This is the principal reason why the liquid lines of descent calculated by Toplis and Carroll (1996) all show strong iron depletion past Fe–Ti oxide crystallization.

The ilmenite modes are unlikely to remain constant as the liquid is depleted in TiO_2. Two models illustrated in Fig. 15 take this into consideration (see Appendix A for details). Model B assumes constant magnetite and initially dominating and decreasing ilmenite modes as crystallization temperature and liquid remaining decrease. An alternative Model A assumes decreasing modes for both magnetite and ilmenite and will result in marked FeO and restricted SiO_2 increases past the appearance of Fe–Ti oxides. Model D is based on the results of Toplis and Carroll (1996) and shows in a rapid drop in FeO and increase in SiO_2.

The model calculations (Fig. 15) reinforce the expectations that the absolute and relative Fe–Ti oxide modes are the principal control on the late stage evolution of the Skaergaard intrusion. Only for very small modal contents of Fe–Ti oxide minerals in the solid fractionate (Model A) will the resultant liquid be able to evolve toward increasing iron and decreasing (or relatively constant) silica contents. Models that assume Fe–Ti oxide modes consistent with the experiments and the observed modes (Models B and C) all show relatively constant to slightly increasing iron content after the start of Fe–Ti oxide crystallization. Models with relatively high Fe–Ti oxide modes (Model D) suggest strong depletion of iron. Silica enrichment appears to be positively correlated with Fe–Ti oxide content (Fig. 15); the higher Fe–Ti oxide contents the higher silica in the late stage melts.

Small variations in parental melt composition can change plagioclase/pyroxene ratios. This is suggested by the experiments of Toplis and Carroll (1995) that gave a plagioclase/augite ratio of 1.20 (by weight) on a composition (SC1, Table 1) with slightly higher Al_2O_3 content than dike *Cm* (Table 1) for which the plagioclase/augite ratio of 1.04 has been well established by the present experiments. The effect of variable plagioclase/augite ratio of the solid fractionate is illustrated in Fig. 16. The appearance of magnetite has been calculated according to Ariskin and Barmina (1999). The calculations show that Fe–Ti oxide saturation occurs at increasingly higher total FeO contents with increasing plagioclase in the solid fractionate (Fig. 16). The reason is that magnetite saturation is not only dependent on iron concentration, but also depends on SiO_2, TiO_2, and P_2O_5 in addition to f_{O_2} (Toplis et al., 1994; Ariskin and Barmina, 1999). It is also observed that the delay, referenced to the SiO_2 content, in the commencement of iron depletion increases with increasing modal plagioclase.

The experimentally determined cotectic proportions of plagioclase and pyroxene (1.04) are slightly lower than shown by the Skaergaard layered series gabbros. The observed average plagioclase/pyroxene ratio of LZ

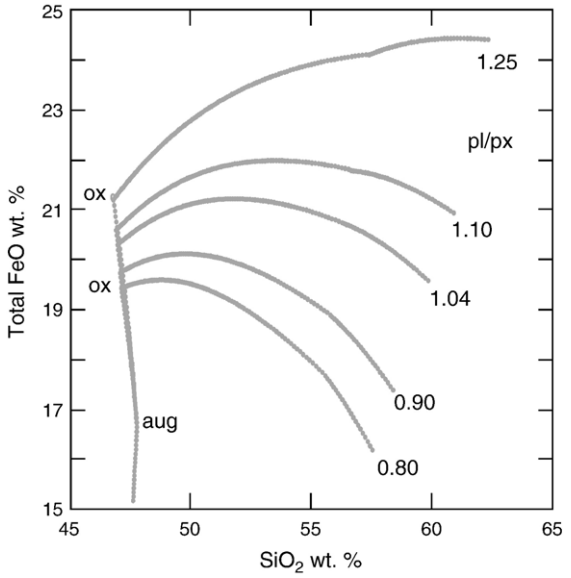

Fig. 16. The effects of plagioclase/pyroxene ratio for fractional crystallization open with respect to oxygen and referenced to the FMQ oxygen buffer. The crystallization orders used in the calculations are similar to those used in Fig. 13, except that pigeonite has been excluded. The income of Fe–Ti oxide minerals is based on the equation given by Ariskin and Barmina (1999).

gabbros is 1.15 (on a weight basis), despite large variations and a sampling restricted to certain, perhaps not representative, rhythmically layered gabbros (Wager and Deer, 1939; Wager and Brown, 1967; Maaløe, 1974, 1976b, 1978; Conrad and Naslund, 1989; Sørensen, 1995). The average modal silicate content of the MZ and UZ appears to be relatively similar to that for the LZ and does not suggest stratigraphically controlled variation in the modal content of the gabbros, such as would have been expected from build-up of volatile components with low melt fraction remaining. Thus, the combined effect of progressively reduced crystallization conditions (to one log units below FMQ) and a relatively high plagioclase content of the fractionate did result in significant iron and silica enrichments in the liquid. The absolute iron concentrations may have reached UZc levels approaching values estimated by Tegner (1997, 26 wt.% FeO); however, it is clear from Fig. 16 that silica enrichment was also a prominent factor in the evolution of the Skaergaard liquid.

5.5. Crystallization orders and parental magma

The crystallization (or melting) orders obtained in the experiments on the Skaergaard dikes are, in general, consistent with the cumulus zone divisions and thus to a certain extent applicable to understanding the Skaergaard intrusion. The experiments mostly show the crystallization order plagioclase; olivine; augite; Fe–Ti oxides. Pigeonite appears to replace olivine after (FMQ; Table 2; Snyder et al., 1993) or before (MW; Hoover, 1989a) the appearance of Fe–Ti oxides. With a few exceptions, this crystallization order reproduces the Skaergaard zone divisions from LZa to MZ. Anorthositic cumulates are not exposed in the LS, but may be present at depth in the HZ (Maaløe, 1976b). The status of pigeonite is uncertain and in part can be the result of subsolidus reequilibration (McBirney, 1989; McBirney and Naslund, 1990). Brown et al. (1957) described pigeonite coexisting with olivine in LZb and suggested that this phase continued after the disappearance of olivine in the MZ. The present experimental results suggest a reaction relationship between olivine and liquid to produce pigeonite, in conflict with the apparent appearance of pigeonite in equilibrium with olivine in LZb (Brown et al., 1957; Wager and Brown, 1967).

The similarities between the experimental phase equilibria and LS gabbros extend to the detailed phase compositions. The most primitive cumulates occur in the early marginal border series and contain cumulus olivine (Fo_{70}) and plagioclase (An_{71}) (Maaløe, 1976b; Nwe, 1976). These compositions are slightly more primitive than those of cumulates in the upper part of the HZ, sampled by the Cambridge drill hole (Maaløe, 1976b; Nwe, 1976), and the lowermost exposed cumulates of LZa (Wager and Brown, 1967; McBirney, 1989). There is a relatively good correspondence between these most primitive rocks and the coexisting mineral compositions experimentally produced in this study as well as those of Hoover (1989a) and Toplis and Carroll (1995). Furthermore, the forward modeling based on dike composition *Cm* reproduces quite well the observed cryptic variation in the LS (Thy and Lesher, 1996), with the exception of a slight deviation for LZ olivine believed to result from reequilibration with trapped liquid (cf., Barnes, 1986; Cawthorn et al., 1992).

In the case where direct experimental evidence is available, such as for the Skaergaard dikes (Table 2), the modeling is straightforward. In order to produce the slightly early silica depletion, suggested for the Skaergaard intrusion prior to Fe–Ti oxide saturation (McBirney and Naslund, 1990), the relative concentration of silica in the parental melt is a critical factor (Fig. 17). Parental melts with less than 49–50 wt.% SiO_2 will produce slightly early silica depletion after augite saturation. In contrast, parental melts with above 49–50 wt.% SiO_2 will produce early silica enrichment. Another important factor for controlling the relative

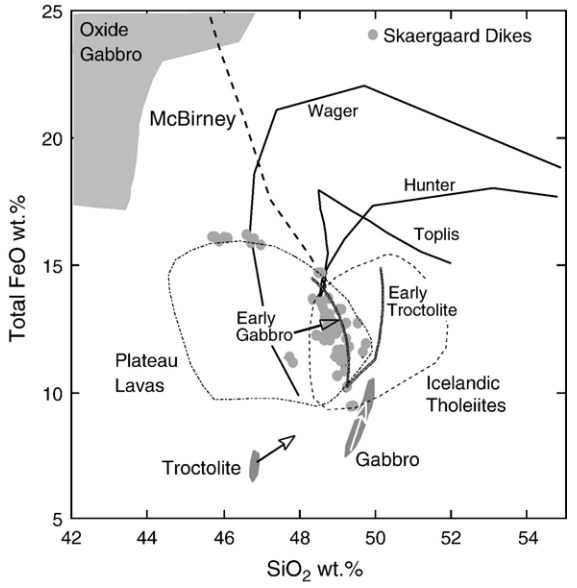

Fig. 17. Total FeO versus SiO_2 (wt.%) for various models of the Skaergaard liquid line of descent (Wager, 1960; Hunter and Sparks, 1987; McBirney and Naslund, 1990; Toplis and Carroll, 1996). Also shown are the general variation of East Greenland plateau lavas (Larsen et al., 1999) and Icelandic tholeiites. The curved marked 'early gabbro' and 'early troctolite' are calculated assuming a low FeO Skaergaard dike and the initial crystallization of either a troctolite or gabbro (note that oxide crystallization has been suppressed in these later two models). The general fields for calculated cumulates (troctolite, gabbro, oxide gabbro) are shown assuming no trapped liquid.

depletion or enrichment of silica is the appearance of augite. The reason is that crystallization of augite will shift the solid fractionate towards higher silica and consequently deflect an initial silica enrichment trend toward silica depletion with increasing iron (Fig. 17). An early appearance of augite will thus enhance silica depletion prior to Fe–Ti oxide saturation, but will have only a minor effect on the liquid line of descent past Fe–Ti oxide crystallization.

6. Conclusions

- The experimental melting order for the evolved ferrobasaltic Skaergaard dikes duplicates the LZ and MZ zone division in the layered series of the Skaergaard intrusion reasonable well.
- Forward modeling of LZa troctolite fractionation drives the residual liquid toward increasing iron with slight increase in silica.
- Fractionation of gabbro adjusts the liquid descent to slightly decreasing silica with continued increase in iron. The amount of silica decrease is restricted by the income of augite in LZb.
- The appearance of Fe–Ti oxide minerals and fractionation of oxide gabbros in LZc strongly influence the Skaergaard liquid line of descent. The iron concentration levels at which Fe–Ti oxide minerals appear are dependent on f_{O_2}.
- Fractionation under conditions of constant oxygen results in an increase in f_{O_2} to about 0.1 log unit above FMQ at the beginning of LZc. This does not justify speculations that large differences in oxide modes would be the result of fractionation under conditions open (experimental results) or closed (Skaergaard) with respect to exchange of oxygen. The experimental results are therefore reasonably applicable for modeling of the Skaergaard LZ gabbros.
- The forward modeling shows that the fractionation of Fe–Ti oxides from LZc markedly deflects the silica variation to show strong increase with fractionation. Modeling based on the new experimental results suggests that iron can continue to increase through LZc and into MZ, past the appearance of Fe–Ti oxides, and supports the possibility that iron may have continued to increase into UZ.
- The forward modeling using the experimentally determined mineral modes suggests only modest MZ and UZ deviations from the FMQ oxygen buffer. This contrasts with the strong UZ drop in f_{O_2} ($\sim$2 log units below FMQ) that has previously been suggested. Such f_{O_2} variation requires relatively high total modal content of Fe–Ti oxides ($>$20 wt.%) and dominating magnetite over ilmenite.
- There is no support in the forward modeling for silica depletion past Fe–Ti oxide crystallization in the MZ and UZ. Only for very small amounts of Fe–Ti oxide minerals, well below the experimental results and the observed gabbro modes, will silica continue to decrease well into the UZ.

Acknowledgement

The U.S. Natural Science Foundation (NSF/EAR-0208075 CEL) has provided funding for this project. The Danish Lithosphere Center, University of Copenhagen in part supported visits by PT and CEL to the Skaergaard intrusion during the summers of 1995 and 2000. Critical comments by C. Tegner, S. Maaløe, and J.C.Ø. Andersen on various versions of this manuscript have been very helpful. Reviews by Mike Toplis and Richard Wilson helped us improve the present discussion.

Appendix A. Summary of quantitative crystallization model

Temperature (T °C, wt.% oxides)
$T = 995.35 + 26.365 \times MgO$
Equilibrium Modes (weight fractions; F = liquid weight fraction)
$ol = 0.10474 - 0.08812 \times F$
$ol = 0.01479 + 0.05025 \times F$ (pi stable)
$pl = 0.47673 - 0.44462 \times F$
$au = 0.39024 - 0.42822 \times F$
$pi = 0.12487 - 0.19888 \times F$
$il = 0.10163 - 0.13180 \times F$ or
$il = 0.05377 + 0.01076 \times F - 0.05201 \times F^2 - 0.07860 \times F^3$
$mt = 0.05180 - 0.07217 \times F$ or
$mt = 0.03267 - 0.01198 \times F + 0.02401 \times F^2 - 0.10278 \times F^3$
The modes are normalized to 1 for appropriate assemblages.
Instantaneous Modes (weight fractions; F = liquid weight fraction)
Pl + Ol:
$ol = 0.264$
$pl = 0.737$
Pl ± Ol + Au ± Pi ± (il + mt):
$ol = 0.0881$
$ol = 0$ (pi stable)
$pl = 0.445$
$au = 0.428$
$pi = 0.199$
$il = 0.1380$ or
$il = 0.10638 \times F + 0.23688 \times F^2 - 0.010231$
$mt = 0.0722$ or
$mt = 0.011746 - 0.044932 \times F + 0.30834 \times F^2$
The modes are normalized to 1 for appropriate assemblage.
Mineral Compositions
Olivine (wt.% oxides; T °C):
All iron calculate as FeO
TiO_2, Al_2O_3, Na_2O, K_2O, P_2O_5 all zero
$KD^{ol/liq}$ (FeO/MgO) $= 0.75284 - 3.7209 \times 10^{-4} \times T$ (mol)
DMnO (ol/liq) = 1.65
DCaO (ol/liq) $= 0.29958 - 2.2161 \times 10^{-4} \times T$
DMgO (ol/liq) $= 18.568 - 0.010787 \times T$
Plagioclase (wt.% oxides; T °C):
All iron calculated as FeO
MnO, P_2O_5 both zero
$KD^{pl/liq}$ (Na_2O/CaO) $= 7.6061 - 5.662\ 10^{-3} \times T$ (mol)
$DTiO_2$ (pl/liq) $= 1.9006 \times 10^{-4} \times T - 0.18053$
DFeO (pl/liq) $= 4.1105 \times 10^{-4} \times T - 0.39589$
DMgO (pl/liq) = 0.035
DK_2O (pl/liq) $= 1.2238 - 8.1889 \times 10^{-4} \times T$
DCaO (pl/liq) = 1.25
Augite (wt.% oxides; T °C):
$Fe_2O_3 = 0.18 \times FeO^{total}$
$FeO = FeO^{total} - 0.9 \times Fe_2O_3$
K_2O, P_2O_5 both zero
$KD^{px/liq}$ (FeO/MgO) $= 5.0223 \times 10^{-4} \times T - 0.35403$ (mol)
$DTiO_2$ (px/liq) $= 1.9926 \times 10^{-3} \times T - 1.9698$
DAl_2O_3 (px/liq) $= 1.1368 \times 10^{-3} \times T - 1.0572$
DFe_2O_3 (px/liq) $= 2.312 - 0.0014 \times T$
DMnO (px/liq) $= 8.2437 - 0.0063882 \times T$
DCaO (px/liq) $= 6.9699 - 0.0045383 \times T$
DNa_2O (px/liq) $= 1.5064 \times 10^{-4} \times T - 0.068287$
DMgO (px/liq) $= 33.704 - 0.02706 \times T$
Pigeonite (wt.% oxides):
All iron calculated as FeO
K_2O, P_2O_5 both zero
$KD^{px/liq}$ (FeO/MgO) = 0.262
$DTiO_2$ (px/liq) = 0.162
DAl_2O_3 (px/liq) = 0.093
DMnO (px/liq) = .691
DCaO (px/liq) = 0.639
DNa_2O (px/liq) = 0.038
DMgO (px/liq) = 5.312
Ilmenite (wt.% oxides; ΔFMQ log units above or below FMQ buffer):
SiO_2, Na_2O, K_2O, P_2O_5 all zero
$TiO_2 = 48.5$ (constant, Supplementary Dataset 4 (Table 7))
$FeO^{total} = 43.8$ (constant, Supplementary Dataset 4 (Table 7))
$Fe_2O_3 = 8.7673 + 3.3636 \times \Delta FMQ$ (based on Toplis and Carroll, 1995)
$FeO = FeO^{total} - Fe2O3 \times 0.9$
DAl_2O_3 (il/liq) = 0.0357
DMgO (il/liq) = 1.075
DMnO (il/liq) = 1.684
DCaO (il/liq) = 0.0175
Magnetite (wt.% oxides; ΔFMQ log units above or below FMQ buffer):
SiO_2, Na_2O, K_2O, P_2O_5 all zero
$TiO_2 = 23.8$ (constant, Supplementary Dataset 4 (Table 7))
$FeO^{total} = 48.4$ (constant, Supplementary Dataset 4 (Table 7))
$Fe_2O_3 = 21.413 + 8.0348 \times \Delta FMQ$ (based on Toplis and Carroll, 1995)
$FeO = FeO^{total} - Fe_2O_3 \times 0.9$
DAl_2O_2 (mt/liq) = 0.225
DMgO (mt/liq) = 1.003
DMnO (mt/liq) = 1.361
DCaO (mt/liq) = 0.041

Appendix B. Supplementary data

Supplementary data associated with this article can be found, in the online version, at doi:10.1016/j.lithos.2006.03.031.

References

Andersen, D.J., Lindsley, D.H., 1988. Internally consistent solution models for Fe–Mg–Mn–Ti oxides: Fe–Ti oxides. Am. Mineral. 73, 714–726.
Andreasen, R., Peate, D.W., Brooks, C.K., 2004. Magma plumbing systems in large igneous provinces: inferences from cyclical variations in Palaeogene East Greenland basalts. Contrib. Mineral. Petrol. 147, 438–452.
Ariskin, A.A., 1999. Phase equilibria modeling in igneous petrology; use of COMAGMAT model for simulating fractionation of fero-basaltic magmas and the genesis of high-alumina basalt. J. Volcanol. Geotherm. Res. 90, 115–162.
Ariskin, A.A., 2002. Geochemical thermometry of the layered series rocks of the Skaergaard intrusion. Petrology 10, 495–518 (translated from Petrologiya 10, 563–588, 2002).
Ariskin, A.A., Barmina, G.S., 1999. An empirical model for the calculation of spinel-melt equilibria in mafic igneous systems at

atmospheric pressure: 2 Fe–Ti oxides. Contrib. Mineral. Petrol. 134, 251–263.
Baker, D.R., Eggler, D.H., 1987. Compositions of anhydrous and hydrous melts coexisting with plagioclase, augite, and olivine or low-Ca pyroxene from 1 atm to 8 kbar: application to the Aleutian volcanic center of Atka. Am. Mineral. 72, 12–28.
Barnes, S.J., 1986. The effect of trapped liquid crystallization on cumulus mineral compositions in layered intrusions. Contrib. Mineral. Petrol. 93, 524–531.
Biggar, G.M., 1972. Diopside, lithium metasilicate and the 1968 temperature scale. Mineral. Mag. 38, 741–770.
Biggar, G.M., 1974. Phase equilibrium studies of chilled margins of some layered intrusions. Contrib. Mineral. Petrol. 46, 159–167.
Bowen, N.L., 1928. The Evolution of the Igneous Rocks. Princeton University Press, Princeton.
Brooks, C.K., 1979. Geomorphological observations at Kangerdlugssuaq, East Greenland. Meddelelser om Grønland. Geosciences 1, 1–21.
Brooks, C.K., Nielsen, T.F.D., 1978. Early stages in the differentiation of the Skaergaard magma as revealed by closely related suite of dike rocks. Lithos 11, 1–14.
Brooks, C.K., Nielsen, T.F.D., 1990. A discussion of Hunter and Sparks (Contrib Mineral Petrol 95:451–461). Contrib. Mineral. Petrol. 104, 235–247.
Brown, G.M., Vincent, E.A., 1963. Pyroxenes from the late stages of fractionation of the Skaergaard intrusion, East Greenland. J. Petrol. 4, 175–197.
Brown, G.M., Vincent, E.A., Brown, P.E., 1957. Pyroxenes from the early and middle stages of fractionation of the Skaergaard intrusion, East Greenland. Mineral. Mag. 31, 511–543.
Bryan, W.B., Finger, L.W., Chayes, F., 1969. Estimating proportions in petrographic mixing equations by least squares approximations. Science 163, 926–927.
Buddington, A.F., Lindsley, D.H., 1964. Iron-titanium oxide minerals and synthetic equivalents. J. Petrol. 5, 310–357.
Campbell, I.H., Roeder, P.L., Dixon, J.M., 1978. Plagioclase buoyancy in basaltic liquids as determined with the centrifuge furnace. Contrib. Mineral. Petrol. 67, 369–377.
Carmichael, I.S.E., 1964. The petrology of Thingmuli, a tertiary volcano in eastern Iceland. J. Petrol. 5, 435–460.
Cawthorn, R.G., Sander, B.K., Jones, I.M., 1992. Evidence for the trapped liquid shift effect in the Mount Ayliff intrusion, South Africa. Contrib. Mineral. Petrol. 111, 194–202.
Chayes, F., 1970. On estimating the magnitude of the hidden zone and the compositions of the residual liquids of the Skaergaard layered series. J. Petrol. 11, 1–14.
Conrad, M.E., Naslund, H.R., 1989. Modally-graded rhythmic layering in the Skaergaard intrusion. J. Petrol. 30, 251–269.
Fenner, C.N., 1929. The crystallization of basalt. Am. J. Sci. 18, 225–253.
Ford, C.E., 1981. Parental liquids of the Skaergaard intrusion cumulates. Nature 291, 21–25.
Frost, B.R., Lindsley, 1992. Equilibria among Fe–Ti oxides, pyroxenes, olivine, and quartz: Part II. Application. Am. Mineral. 77, 1004–1020.
Frost, B.R., Lindsley, D.H., Andersen, D.J., 1988. Fe–Ti oxide-silicate equilibria: assemblages with fayalitic olivine. Am. Mineral. 73, 727–740.
Furman, T., Frey, F.A., Meyer, P.S., 1992. Petrogenesis of evolved basalts and rhyolites at Austurhorn, southeastern Iceland: the role of fractional crystallization. J. Petrol. 33, 1405–1445.
Gee, L., Sack, R.O., 1988. Experimental petrology of melilite nephelinites. J. Petrol. 29, 1233–1255.
Ghiorso, M.S., 1997. Thermodynamic models of igneous processes. Annu. Rev. Earth Sci. 25, 221–241.
Ghiorso, M.S., Carmichael, I.S.E., 1985. Chemical mass transfer in magmatic processes II: applications in equilibrium crystallization, fractionation and assimilation. Contrib. Mineral. Petrol. 90, 121–141.
Ghiorso, M.S., Carmichael, I.S.E., 1987. Modeling magmatic systems: petrologic applications. Rev. Miner. 17, 467–499.
Ghiorso, M.S., Sack, R.O., 1995. Chemical mass transfer in magmatic processes: IV. A revised and internally consistent thermodynamic model for the interpolation and extrapolation of liquid-solid equilibria in magmatic systems at elevated temperatures and pressures. Contrib. Mineral. Petrol. 119, 197–212.
Govindaraju, K., 1989. 1989 compilation of working values and sample description for 272 geostandards. Geostand. Newsl. 13, 1–113.
Grove, T.L., 1981. Use of FePt alloys to eliminate the iron loss problem in 1-atmosphere gas mixing experiments: theoretical and practical considerations. Contrib. Mineral. Petrol. 78, 298–304.
Grove, T.L., Baker, M.B., 1984. Phase equilibrium controls on the tholeiitic versus calc-alkaline differentiation trends. J. Geophys. Res. 89, 3253–3274.
Grove, T.L., Bryan, W.B., 1983. Fractionation of pyroxene-phyric MORB at low pressure: an experimental study. Contrib. Mineral. Petrol. 84, 293–309.
Grove, T.L., Juster, T.C., 1989. Experimental investigations of low-Ca pyroxene stability and olivine-pyroxene-liquid equilibria at 1-atm in natural basaltic and andesitic liquids. Contrib. Mineral. Petrol. 103, 287–305.
Grove, T.L., Gerlach, D.C., Sando, T.W., 1982. Origin of calc-alkaline series lavas at Medicine Lake Volcano by fractionation, assimilation and mixing. Contrib. Mineral. Petrol. 80, 160–182.
Hamilton, D.L., Burnham, C.W., Osborn, E.F., 1964. The solubility of water and effects of oxygen fugacity and water content on crystallization in mafic magmas. J. Petrol. 5, 21–39.
Hanghøj, K., Rosing, M.T., Brooks, C.K., 1995. Evolution of the Skaergaard magma: evidence from crystallized melt inclusions. Contrib. Mineral. Petrol. 120, 265–269.
Hill, R., Roeder, P., 1974. The crystallization of spinel from basaltic liquid as a function of oxygen fugacity. J. Geol. 82, 709–729.
Hoover, J.D., 1978. Melting relations of a new chilled margin sample from the Skaergaard intrusion. Carnegie Inst. Wash. Year Book 77, 739–743.
Hoover, J.D., 1989a. The chilled marginal gabbro and other contact rocks of the Skaergaard intrusion. J. Petrol. 30, 441–476.
Hoover, J.D., 1989b. Petrology of the marginal border series of the Skaergaard intrusion. J. Petrol. 30, 399–439.
Hoover, J.D., Irvine, T.N., 1977. Liquidus relations and Fe–Mg partitioning of part of the system Mg_2SiO_4–Fe_2SiO_4–$CaMgSi_2O_6$–$CaFeSi_2O_6$–$CaMgSi_2O_6$–$KAlSi_3O_8$–SiO_2. Carnegie Inst. Wash. Year Book 77, 774–784.
Hunter, R.H., Sparks, R.S.J., 1987. The differentiation of the Skaergaard intrusion. Contrib. Mineral. Petrol. 95, 451–461.
Hunter, R.H., Sparks, R.S.J., 1990. The differentiation of the Skaergaard intrusion, reply. Contrib. Mineral. Petrol. 104, 248–254.
Irvine, T.N., 1970. Crystallization sequences in the Muskox intrusion and other layered intrusions. 1, olivine-pyroxene-plagioclase relations. Spec. Publ.-Geol. Soc. S. Afr. 1, 441–476.

Irvine, T.N., Andersen, J.C.Ø., Brooks, C.K., 1998. Included blocks (and blocks within blocks) in the Skaergaard intrusion: geological relations and the origins of rhythmic modally graded layers. Geol. Soc. Amer. Bull. 110, 1398–1447.

Jakobsen, J.K., Veksler, I.V., Tegner, T., Brooks, C.K., 2005. Immiscible iron- and silica-rich melts in basalt petrogenesis documented in the Skaergaard intrusion. Geology 33, 885–888.

Jang, Y.D., Naslund, H.R., 2003. Major and trace element variation in ilmenite in the Skaergaard intrusion: petrologic implications. Chem. Geol. 193, 109–125.

Jang, Y.D., Naslund, H.R., McBirney, A.R., 2001. The differentiation trend of the Skaergaard intrusion and the timing of magnetite crystallization: iron enrichment revisited. Earth Planet. Sci. Lett. 189, 189–196.

Juster, T.C., Grove, T.L., Perfit, M.R., 1989. Experimental constraints on the generation of FeTi basalts, andesites, and rhyodacites at the Galapagos spreading center, 85°W and 95°W. J. Geophys. Res. 94, 9251–9274.

Kilinc, A., Carmichael, I.S.E., Rivers, M.L., Sack, R.O., 1983. The ferric-ferrous ratio of natural silicate liquids equilibrated in air. Contrib. Mineral. Petrol. 83, 136–140.

Langmuir, C.H., Hanson, G.N., 1981. Calculating mineral-melt equilibria with stoichiometry, mass balance, and single-component distribution coefficients. In: Newton, R.C., Navrotsky, A., Wood, B.J. (Eds.), Thermodynamics of Minerals and Melts. Springer-Verlag, New-York, pp. 247–271.

Larsen, L.M., Watt, W.S., Watt, M., 1989. Geology and petrology of the lower Tertiary plateau basalts of the Scoresby Sund region, East Greenland. Bull.-Grønl. Geol. Unders. 157 (164 pp.).

Larsen, R.B., Brooks, C.K., Bird, D.K., 1992. Methane-bearing, aqueous, saline solutions in the Skaergaard intrusion, East Greenland. Contrib. Mineral. Petrol. 112, 428–437.

Larsen, L.M., Waagstein, R., Pedersen, A.K., Story, M., 1999. Trans-Atlantic correlation of the Palaeogene volcanic successions in the Faeroe Islands and East Greenland. J. Geol. Soc. (Lond.) 156, 1081–1095.

Lindsley, D.H., Brown, G.M., Muir, I.D., 1969. Conditions of the ferrowollastonite-ferrohedenbergite inversion in the Skaergaard intrusion, East Greenland. Spec. Pap.-Miner. Soc. Am. 2, 193–201.

Longhi, J., 1991. Comparative liquidus equilibria of hypersthene-normative basalts at low pressure. Am. Mineral. 76, 785–800.

Maaløe, S., 1974. The zoned plagioclase of the Skaergaard intrusion. PhD thesis, Univ. Copenhagen. 190 pp.

Maaløe, S., 1976a. Quantitative aspects of fractional crystallization of major elements. J. Geol. 84, 81–96.

Maaløe, S., 1976b. The zoned plagioclase of the Skaergaard intrusion, East Greenland. J. Petrol. 17, 398–419.

Maaløe, S., 1978. The origin of rhythmic layering. Mineral. Mag. 42, 337–345.

Macdonald, R., Sparks, R.S.J., Sigurdsson, H., Mattey, D.P., McGarvie, D.W., Smith, R.L., 1987. The 1875 eruption of Askja volcano, Iceland: combined fractional crystallization and selective contamination in the generation of rhyolitic magma. Mineral. Mag. 51, 183–202.

Macdonald, R., McGarvie, D.W., Pinkerton, H., Smith, R.L., Palacz, Z.A., 1990. Petrogenic evolution of the Torfajökull volcanic complex, Iceland: I. Relationship between the magma types. J. Petrol. 31, 429–459.

McBirney, A.R., 1975. Differentiation of the Skaergaard intrusion. Nature 253, 691–694.

McBirney, A.R., 1989. The Skaergaard layered series: I. Structure and average compositions. J. Petrol. 30, 363–397.

McBirney, A.R., 1995. Mechanisms of differentiation in the Skaergaard intrusion. J. Geol. Soc. (Lond.) 152, 421–435.

McBirney, A.R., 1996. The Skaergaard intrusion. In: Cawthorn, R.G. (Ed.), Layered Intrusions. Elsevier, Amsterdam, pp. 147–180.

McBirney, A.R., 1998. Iron in plagioclase as a monitor of the differentiation of the Skaergaard intrusion: a discussion of Christian Tegner (Contrib Mineral Petrol 128, 45–51). Contrib. Mineral. Petrol. 132, 103–105.

McBirney, A.R., Naslund, H.R., 1990. The differentiation of the Skaergaard intrusion. A discussion of Hunter and Sparks (Contrib Mineral Petrol 95:451–461). Contrib. Mineral. Petrol. 104, 235–247.

Morse, S.A., 1990. A discussion of Hunter and Sparks (Contrib Mineral Petrol 95:5451–461). Contrib. Mineral. Petrol. 104, 240–244.

Morse, S.A., Lindsley, D.H., Williams, R.J., 1980. Concerning intensive parameters in the Skaergaard intrusion. Am. J. Sci. 280-A, 159–170.

Muan, A., Osborn, E.F., 1956. Phase equilibria at liquidus temperatures in the system MgO–FeO–Fe_2O_3–SiO_2. Am. Ceram. Soc. J. 39, 121–140.

Myers, J.S., 1980. Structure of the coastal dyke swarm and associated plutonic intrusions of East Greenland. Earth Planet. Sci. Lett. 46, 407–418.

Naslund, H.R., 1984. Petrology of the upper border series of the Skaergaard intrusion. J. Petrol. 25, 185–212.

Nicholson, H., Condomines, M., Fitton, J.G., Fallick, A.E., Grönvold, K., Rogers, G., 1991. Geochemical and isotopic evidence for crustal assimilation beneath Krafla, Iceland. J. Petrol. 32, 1005–1020.

Nielsen, T.F.D., 1978. The Tertiary dike swarms of the Kangerdlugssuaq area, East Greenland. An example of magmatic development during continental break-up. Contrib. Mineral. Petrol. 67, 63–78.

Nielsen, R.L., 1988. A model for the simulation of combined major and trace element liquid lines of descent. Geochim. Cosmochim. Acta 52, 27–38.

Nielsen, T.F.D., 2004. The shape and volume of th eSkaergaard intrusion, Greenland: implications for mass balance and bulk composition. J. Petrol. 45, 507–530.

Nielsen, T.F.D., Brooks, C.K., 1981. The E Greenland rifted continental margin: an examination of the coastal flexure. J. Geol. Soc. (Lond.) 138, 559–568.

Nwe, Y.Y., 1976. Electron-probe studies of the earlier pyroxenes and olivines from the Skaergaard intrusion, East Greenland. Contrib. Mineral. Petrol. 55, 105–126.

Osborn, E.F., 1959. Role of oxygen pressure in the crystallization and differentiation of basaltic magma. Am. J. Sci. 257, 609–647.

Osborn, E.F., 1962. Reaction series for subalkaline igneous rocks based on different oxygen pressure conditions. Am. Mineral. 47, 211–226.

Papike, J.J., Cameron, K.L., Baldwin, K., 1974. Amphiboles and pyroxenes: characterization of other than quadrilateral components and estimates of ferric iron from microprobe data. Abstr. Programs-Geol. Soc. Am. 6, 1053–1054.

Presnall, D.C., 1966. The join forsterite-diopside-iron oxide and its bearing on the crystallization of basaltic and ultramafic magmas. Am. J. Sci. 264, 753–809.

Roeder, P.L., Emslie, R.F., 1970. Olivine-liquid equilibria. Contrib. Mineral. Petrol. 29, 275–289.

Roeder, P.L., Osborn, E.F., 1966. Experimental data for the system $MgO–FeO–Fe_2O_3–CaAl_2Si_2O_8–SiO_2$ and their petrogenetic implications. Am. J. Sci. 264, 428–480.

Snyder, D.A., Carmichael, I.S.E., 1992. Olivine-liquid equilibria and chemical activities of FeO, NiO, Fe_2O_3, and MgO in natural basic melts. Geochim. Cosmochim. Acta 56, 303–318.

Snyder, D., Carmichael, I.S.E., Wiebe, R.A., 1993. Experimental study of liquid evolution in an Fe-rich, layered mafic intrusion: constraints of Fe–Ti oxide precipitation on the T-f_{O_2} and T-ρ paths of tholeiitic magmas. Contrib. Mineral. Petrol. 113, 73–86.

Sørensen, K.B., 1995. Textural and chemical evolution of the Fe–Ti oxide minerals during late-and post magmatic cooling of the Skaergaard intrusion, East Greenland. MS thesis, Univ. Copenhagen.

Tegner, C., 1997. Iron in plagioclase as a monitor of the differentiation of the Skaergaard intrusion. Contrib. Mineral. Petrol. 128, 45–51.

Thy, P., 1992. Low-pressure melting relations of a basalt from Hole 797C in the Yamato basin of the Japan Sea. In: Tamaki, K., Suyehiro, K., Allan, J., McWilliams, M., et al. (Eds.), Proceedings of the Ocean Drilling Program, Scientific Results, vol. 127/128. Ocean Drilling Program, College Station, pp. 861–868.

Thy, P., Lesher, C.E., 1993. Melting experiments on Kraemer Island dikes and their implications for the parental magma and differentiation of the Skaergaard intrusion. EOS Trans.-Am. Geophys. Union 74, 622.

Thy, P., Lesher, C.E., 1996. Experimental modeling of Skaergaard cumulates. EOS Trans.-Am. Geophys. Union 77, 822.

Thy, P., Lofgren, G.E., 1992. Experimental constraints on the low-pressure evolution of transitional and mildly alkalic basalts: multisaturated liquids and coexisting augites. Contrib. Mineral. Petrol. 112, 196–202.

Thy, P., Lofgren, G.E., 1994. Experimental constraints on the low-pressure evolution of transitional and mildly alkalic basalts: the effect of Fe–Ti oxide minerals and the origin of basaltic andesites. Contrib. Mineral. Petrol. 116, 340–351.

Thy, P., Lesher, C.E., Fram, M.S., 1998. Low pressure experimental constraints on the evolution of basaltic lavas from Site 917, southeast Greenland continental margin. In: Saunders, A.D., Larsen, H.C., Wise, S.W. (Eds.), Proceedings of the Ocean Drilling Program, Scientific Results, vol. 152. Ocean Drilling Program, College Station, pp. 359–372.

Thy, P., Lesher, C.E., Mayfield, J.D., 1999. Low-pressure emelting studies of basalt and basaltic andesite from the southeast Greenland continental margin and the origin of dacites at Site 917. In: Larsen, H.C., Duncan, R.A., Allan, J.F., Brooks, K. (Eds.), Proceedings of the Ocean Drilling Program, Scientific Results, vol. 163. Ocean Drilling Program, College Station, pp. 95–112.

Tilley, C.E., Yoder Jr., H.S., Schairer, J.F., 1963. Melting relations of basalts. Carnegie Inst. Wash. Year Book 62, 77–84.

Toplis, M.J., 2005. The thermodynamics of iron and magnesium partitioning between olivine and liquid; criteria for assessing and predicting equilibrium in natural and experimental systems. Contrib. Mineral. Petrol. 149, 22–39.

Toplis, M.J., Carroll, M.R., 1995. An experimental study of the influence of oxygen fugacity on Fe–Ti oxide stability, phase relations, and mineral-melt equilibria in ferro-basaltic systems. J. Petrol. 36, 1137–1170.

Toplis, M.J., Carroll, M.R., 1996. Differentiation of ferro-basaltic magmas under conditions open and closed to oxygen: implications for the Skaergaard intrusion and other natural systems. J. Petrol. 37, 837–858.

Toplis, M.J., Libourel, G., Carroll, M.R., 1994. The role of phosphorus in basaltic crystallisition processes: an experimental study. Geochim. Cosmochim. Acta 58, 797–810.

Ulmer, P., 1989. The dependence of the Fe^{2+}–Mg cation-partitioning between olivine and basaltic liquid on pressure, temperature and composition. An experimental study to 30 kbar. Contrib. Mineral. Petrol. 101, 261–273.

Ussler, W., Glazner, A.F., 1989. Phase equilibria along a basalt-rhyolite mixing line: implications for the origin of calc-alkaline intermediate magmas. Contrib. Mineral. Petrol. 101, 232–244.

Vincent, E.A., Phillips, R., 1954. Iron-titanium oxide minerals in layered gabbros of the Skaergaard intrusion, East Greenland. Geochim. Cosmochim. Acta 6, 1–26.

Wager, L.R., 1960. The major element variation of the layered series of the Skaergaard intrusion and a re-estimation of the average composition of the hidden layered series and of the successive residual magmas. J. Petrol. 1, 364–398.

Wager, L.R., Brown, G.M., 1967. Layered Igneous Rocks. Freeman, San Francisco.

Wager, L.R., Deer, W.A., 1938. A dyke swarm and crustal flexure in East Greenland. Geol. Mag. 75, 39–46.

Wager, L.R., Deer, W.A., 1939. Geological investigations in East Greenland. Part III. The petrology of the Skaergaard intrusion, Kangerrdlugssuaq, East Greenland. Medd. Grønl. 105 (4) (reissued 1962).

Walker, D., Shibata, T., DeLong, E., 1979. Abyssal tholeiites from the Oceanographer fracture zone: II. Phase equilibria and mixing. Contrib. Mineral. Petrol. 70, 111–125.

Weaver, J.S., Langmuir, C.H., 1990. Calculation of phase equilibria in mineral-melt systems. Comput. Geosci. 16, 1–19.

Williams, R.J., 1971. Reaction constants in the system Fe–MgO–SiO_2–O_2: intensive parameters in the Skaergaard intrusion, East Greenland. Am. J. Sci. 271, 132–146.

Williams, R.J., Mullins, O., 1981. JSC systems using solid ceramic oxygen electrolyte cells to measure oxygen fugacities in gas-mixing systems. NASA Tech. Memo. 58234.

Wood, A.D., 1978. Major and trace element variations in the Tertiary lavas of eastern Iceland with respect to the Iceland geochemical anomaly. J. Petrol. 10, 393–436.

Wright, J.B., 1961. Solid solution relationships in some iron oxide ores of basic igneous rocks. Mineral. Mag. 32, 778–789.